Breakup of nocturnal low-level stratiform clouds during southern West African Monsoon Season

Maurin ZOUZOUA[1], Fabienne LOHOU[2], Paul ASSAMOI[1], Marie LOTHON[2], Véronique YOBOUE[1], Cheikh DIONE[3], Norbert KALTHOFF[4], Bianca ADLER[4], Karmen BABIĆ[4] and Xabier PEDRUZO-BAGAZGOITIA[5]

[1]Laboratoire de Physique de l'atmosphère et de Mécanique des fluides, Université Félix Houphouët Boigny, Abidjan, Côte d'Ivoire
[2]Laboratoire d'Aérologie, Université de Toulouse, CNRS, UPS, Toulouse, France
[3]African Centre of Meteorological Applications for Development, Niamey, Niger
[4]Institute of Meteorology and Climate Research, Karlsruhe Institute of Technology (KIT), Karlsruhe, Germany
[5]Meterology and Air Quality Group, Wageningen University and Research, Wageningen, the Netherlands

Correspondence to: Maurin ZOUZOUA (maurin.zouzoua@aero.obs-mip.fr)

Abstract.

Within the framework of the DACCIWA (Dynamics-Aerosol-Chemistry-Cloud-Interactions over West Africa) project, and based on a field experiment conducted in June and July 2016, we analyse the daytime breakup of the continental low-level stratiform clouds in southern West Africa. We use the observational data gathered during twenty-two precipitation-free occurrences at Savè supersite, in Benin. Our analysis, which starts since the stratiform cloud formation usually at night, focuses on the role played by the coupling between the cloud and the surface in the transition towards shallow convective clouds. It is based on several diagnostics, including Richardson number and various cloud macrophysical properties. The distance between lifting condensation level and cloud base height is used as a criterion of coupling. We also make an attempt to estimate the most predominant terms of the liquid water path budget on early morning.

When the nocturnal low-level stratiform cloud forms, it is decoupled from the surface, except in one case. On early morning, the cloud is found coupled with the surface in nine cases and is remained decoupled in the thirteen other cases. The coupling, which occurs within the four hours after the cloud formation, is accompanied with a cloud base lowering and near-neutral thermal stability in the subcloud layer. Further, at the initial stage of the transition, the stratiform cloud base is slightly cooler, wetter and more homogeneous in the coupled cases. The moisture jump at cloud top is found usually around 2 g kg^{-1}, and the temperature jump within 1-5 K, which is significantly smaller than typical marine stratocumulus, and explained by the monsoon flow environment within which the stratiform cloud develops. No significant difference of liquid water path budget terms was found between the coupled and decoupled cases. In agreement with previous numerical studies, we found that the stratiform cloud maintenance before the sunrise results from the interplay between the predominant radiative cooling, and, the entrainment and large scale subsidence at its top.

Three transition scenarios were observed, depending on the state of the coupling at the initial stage. In the coupled cases, the low-level stratiform cloud remains coupled until its break up. In five of the decoupled cases, the cloud couples with the

surface as the LCL is rising. In the eight remaining cases, the stratiform cloud remains decoupled from the surface all along its life cycle. In case of coupling during the transition, the stratiform cloud base lifts with the growing convective boundary layer roughly between 06:30 and 08:00 UTC. The cloud deck breakup occurring at 11:00 UTC or later leads to the formation of shallow convective clouds. When the decoupling subsists, shallow cumulus clouds form below the stratiform cloud deck

5 between 06:30 and 09:00 UTC. The breakup time in this scenario has a stronger variability, and occurs before 11:00 UTC in most of the cases. Thus we argue that the coupling with the surface during the daytime hours has a crucial role in the low-level stratiform cloud maintenance and in its transition towards shallow convective clouds.

Keywords: Stratiform cloud breakup, surface coupling, liquid water path budget, DACCIWA experiment.

10 **1 Introduction**

The low-level stratiform clouds (LLSC) are Earth's most common cloud type (Wood, 2012). During the West Africa Monsoon season (WAM), the LLSC form frequently at night over a region extending from Guinean coast to several hundred kilometres inland (van der Linden et al., 2015). Figure 1 gives an overview of the horizontal scale of this phenomenon. It shows the low cloud coverage fraction from ECMWF (European Centre for Medium range Weather Forecast) ERA5 re-

15 analyses (Copernicus Climate Change Service, 2019) averaged between 05:00 and 07:00 UTC on 8 July 2016. The expansion of the LLSC over the southern West Africa (SWA) during the night-to-day transition on 07-08 July 2016 was analyzed by Babić et al. (2019a). One can see that the inland affected area spans up to around 11°N. The LLSC coverage persists for many hours during the following day, reducing the incoming solar radiation, and impacting the surface energy budget and related processes such as the diurnal cycle of the atmospheric boundary layer (ABL) (Schuster et al., 2013; Adler

20 et al., 2017; Knippertz et al., 2017). However, the diurnal cycle of those clouds is still poorly represented in numerical weather and climate models (Hannak et al., 2017). Their lifetime is generally underestimated in the numerical simulations causing high incoming solar radiation at the surface (Knippertz et al., 2011). That could be an important factor for which the forecasts of WAM features still have a poor skill (Hannak et al., 2017). Therefore, a better understanding of the processes behind LLSC is useful for modelling purposes. Due to the scarce weather monitoring network over West Africa, the first

25 studies addressing the LLSC over this region were conducted with satellite images and traditional synoptic observation (Schrage and Fink, 2012; van der Linden et al., 2015), as well as with numerical simulations at regional scale (Schuster et al., 2013; Adler et al., 2017; Deetz et al., 2018). They emphasized that the physical processes, spanning from local to synoptic scale such as, horizontal advection of cold air associated to WAM, lifting induced by topography, gravity waves or shear-driven turbulence, are relevant for the LLSC formation during the night.
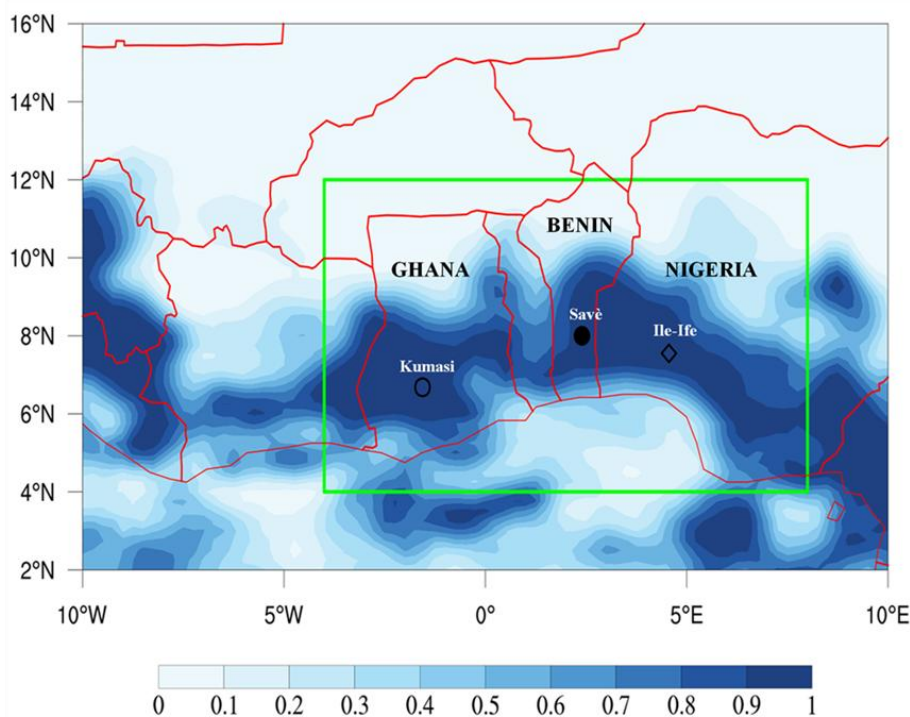
Figure 1. Low cloud coverage fraction over southern-West Africa from ERA5 Re-analyses, averaged between 05:00 and 07:00 UTC on 8 July 2016. The fraction varies from 0 (clear sky) to 1 (totally covered sky). The red lines represent the geopolitical boundaries. The green box delimits the area of interest during DACCIWA field campaign. The black markers indicate the geographical locations of DACCIWA supersites, Kumasi in Ghana (unfilled circle), Savè in Benin (filled circle) and Ile-Ife in Nigeria (unfilled diamond).

During the boreal summer 2016, a field campaign was conducted over SWA within the framework of the European project Dynamics-Aerosol-Chemistry-Cloud Interaction in West Africa (DACCIWA) (Knippertz et al., 2015). The project was developed to study the impact of increasing air pollution on SWA weather and climate. A joint measurement, including aircraft and ground-based campaigns (Flamant et al., 2017; Kalthoff et al., 2018), was performed. The area of interest during this field experiment is indicated in Fig. 1. One of the primary goals of this project was to provide the first high quality and comprehensive dataset in order to conduct a detailed study of the LLSC. To this end, several instruments reporting the evolution of atmospheric conditions and low-level cloud coverage were deployed at three supersites, Kumasi (6.68° N, 1.56° E) in Ghana, Savè (8.00° N, 2.40° W) in Benin, and Ile-Ife (7.55° N, 4.56° W) in Nigeria (Fig. 1).

The comprehensive dataset acquired at Savè supersite allowed the first research studies of LLSC over SWA based on high temporal resolution observations. Adler et al. (2019) and Babić et al. (2019a,b) studied the physical processes which govern the LLSC formation and its maintenance up to the next day. Dione et al. (2019) performed a statistical analysis on the LLSC characteristics and low troposphere dynamic features during the DACCIWA field campaign. The findings of these studies have been generalized and synthesized by Lohou et al. (2020) who also quantified for the first time the impact of the LLSC

on the surface energy budget terms. These observational-based studies focused essentially on the mechanism involved in the formation of LLSC in the WAM context in order to evaluate the hypothesis proposed by earlier research works. They confirmed the role played by the horizontal advection and the vertical wind shear driven by a nocturnal low-level jet (NLLJ) which is among the main features of the WAM (Parker et al., 2005; Lothon et al., 2008). The breakup of the LLSC deck after
5 the sunrise which leads to the transition towards shallow convective clouds has not been well documented yet with the unique DACCIWA dataset. Only Pedruzo-Bagazgoitia et al. (2019) analyzed this transition by the mean of idealized Large Eddy Simulations (LES), inspired by the data collected during the LLSC occurrence on 25-26 June 2016 at Savè supersite. This was the first LES of stratocumulus to shallow cumulus (Sc-Cu) transition over land in SWA.

Our study aims at analyzing the transition from the LLSC to the convective shallow cumulus clouds of twenty-two (22)
10 cases observed at Savè supersite during DACCIWA experiment, addressing the possible scenarios and the involved processes, as far as enabled by the available measurements. This should provide a complementary guidance for numerical model evaluation of this Sc-Cu transition over SWA. The rest of this paper is organized as follow. The section 2 presents a brief state of our knowledge on the diurnal cycle of, the LLSC covering the SWA, and, stratocumulus at other places around the world with a focus on the Sc-Cu transition. The section 3 describes the observational data and the deduced diagnostics
15 used to monitor the LLSC evolution. It also overviews how the contributions of some processes involved in the LLSC diurnal cycle are derived from the measurements. The Section 4 presents the LLSC characteristics just before the sunrise, at the initial stage of the transition. The relative contributions of the physical processes governing the LLSC are estimated. In section 5, the evolution of LLSC on daylight hours is analyzed. Finally, a summary and conclusion are given in section 6.

20 **2 Sate of art**

The diurnal cycle of the LLSC over SWA consists of four main stages: the *stable phase*, the *jet phase*, the *stratus phase* and the *convective phase* (Lohou et al., 2020). The increase of relative humidity within the ABL leading to saturation and their formation is due to the cooling which mainly occurs during the stable and the jet phases. The main process behind this cooling is the horizontal advection of cooler air from Guinea coast, due to the combination of a maritime inflow (MI) (Adler
25 et al., 2017; Deetz et al., 2018) and the NLLJ (Schrage and Fink, 2012; Dione et al., 2019). The onset time and the strength of the NLLJ, as well as the level of background humidity in the ABL, are crucial for the LLSC formation (Babić et al., 2019b). Indeed, from two cases study, Babić et al. (2019b) showed that weaker and later NLLJ onset leads to a reduced cooling, so that the saturation within the ABL may not be reached. The formation of the LLSC marks the end of the jet phase and the beginning of the *stratus phase*. The LLSC base is firstly located around the NLLJ core where the cooling is
30 maximum (Adler et al., 2019; Babić et al., 2019a; Dione et al., 2019; Lohou et al., 2020). During the stratus phase, the maximum of wind speed in the NLLJ is reduced and shifted upward by the turbulent mixing induced by the longwave radiative cooling at the cloud top, typical characteristic of stratocumulus clouds. In addition, the dynamical turbulence

underneath the NLLJ and the convective turbulence due to the cloud top cooling are potential drivers of the coupling between the LLSC and the surface (Adler et al., 2019; Lohou et al., 2020). This dynamical turbulence could also be an important factor for additional cooling below the LLSC base (Babić et al., 2019a). When the LLSC is coupled to the surface, its base coincides quite well with the surface-based lifting condensation level (LCL) (Adler et al., 2019; Lohou et al., 2020).

5 The final *convective phase* of the LLSC diurnal cycle starts after sunrise, when the sensible heat flux becomes larger than 10 W m^{-2}, and ends at the cloud layer breakup (Lohou et al., 2020).

A comprehensive overview on the current state of research on the stratocumulus dynamic is presented by Garratt (1994) and Wood (2012). Such a cloud is regulated through feedbacks between several processes: radiation, precipitation, turbulence fluxes of moisture and heat at cloud base, entrainment and large-scale subsidence at the cloud top. The cloud

10 Liquid Water Path (LWP) budget is considered to disentangle the respective contribution of each process. During night-time, the longwave radiative cooling at the cloud top is the leading process governing the maintenance of the cloud. After the sunrise, the solar radiation comes into play, warming the cloud, and penetrating more and more down to the surface as the Sc breaking occurs. The LES performed by Ghonima et al. (2016) revealed that the effect of turbulent fluxes at cloud base depends upon Bowen ratio (B) at the surface, where B is the ratio of surface sensible flux to latent flux. Low values of B

15 contribute to cloud layer humidification, favouring cloud persistence. In contrast, the predominance of surface sensible heat over latent heat flux ($B > 1$) warms the cloud, leading to its evaporation. The precipitation formation, the large-scale subsidence and entrainment have generally drying and warming effects on the cloud layer (van der Dussen et al., 2016; Wood, 2012).

The Sc-Cu transition in other climatologic regions was the subject of several studies, most of them made over the ocean

20 (e.g. Bretherton et al., 1999; Sandu and Stevens, 2011; Duynkerke et al., 2004; van der Dussen et al., 2016; de Roode et al., 2016), and a few over land (e.g. Ghonima et al., 2016; Price, 1999). In these studies essentially based on numerical simulations, the stratocumulus is initially coupled to the surface with the convective turbulence produced by radiative cooling at the cloud top. They proposed specific mechanisms for the Sc layer breakup, but still based on an enhancement of entrainment warming and drying effect. Over land especially, the main driver is the intensification of the convection within

25 the ABL by the solar heating.

The LES made by Pedruzo-Bagazgoitia et al. (2020) provide an insight on the evolution of a coupled LLSC to surface in terms of involved processes in the SWA Monsoon conditions. Before the sunrise, the cloud-top radiative cooling is the unique positive contribution in LWP budget and is the factor which maintains the cloud layer. The breakup of the cloud deck five hours after the sunrise is mainly due to the progressive decrease of cloud-top cooling, and, increase of cloud-top

30 entrainment negative contribution in LWP budget. About thirty minutes before the stratiform cloud deck breakup, a negative buoyancy flux at the cloud base decouples it from the surface. Later on, a shallow cumulus cloud fully coupled to the surface appears at the convective ABL top. These LES also showed that wind shear at the stratiform cloud top accelerates the Sc-Cu transition by enhancing the impact of entrainment.

3 Data and Methodology

The DACCIWA field experiment took place from 14 June to 31 July 2016. Knippertz et al. (2017) divided this period in four synoptic phases based on the precipitations difference between the coastal (south) and Sudanian-Sahelian areas (north). The second phase (from 22 June to 20 July), so-called post-onset phase, started with a northward shift of rainfall. It is

5   characterized by an increase of low-level cloudiness over SWA. The period from 27 June to 8 July 2016 was characterized by undisturbed monsoon flow over West Africa, especially over DACCIWA investigated area (Knippertz et al., 2017).

The ground sites were located at roughly the same distance from the Guinean coast (200 km in land) but with different topography (Kalthoff et al., 2018). By using the ground-based data, Kalthoff et al. (2018) give an overview of the diurnal cycle of the low-troposphere at the three supersites. The DACCIWA field campaign includes 15 intensive observation

10   periods (IOPs), during which the temporal resolution of the radiosoundings performed at the supersites, especially at Savè supersite, was improved. Each IOP lasted from 17:00 UTC on one day (Day-D) to 11:00 UTC on the following day (Day-D+1).

The ground-based data acquired at Savè supersite on which our investigation is based offer the most complete continuous information on both the cloudy and atmospheric conditions. The instrumentation and the data collected correspond to four

15   published DOI (Derrien et al., 2016; Handwerker et al., 2016; Kohler et al., 2016; Wieser et al., 2016). We analyzed a set of twenty-two LLSC occurrences for which the cloud forms during night and persists at least until sunrise the next day. These cases have been selected over the period from 20 June to 31 July 2016, because of a good data coverage (Dione et al., 2019). Only cases for which the stratus phase, determined by the methodology of Adler et al. (2019), started before 04:00 UTC on day-D+1 have been selected. In addition, for each of the selected cases, no or light precipitation, i.e. less than 1 mm was

20   recorded at surface from 21:00 UTC on day-D to 16:00 UTC on day-D+1. Among these 22 cases, 9 are IOPs, including the 07-08 July 2016 (IOP8) case (Babić et al., 2019a) and the 25-26 June 2016 case (IOP3) (Pedruzo-Bagazgoitia et al., 2020). About 60% of the selected cases occurred between the 26 June and 11 July 2016, a period with pronounced LLSC occurrence over West Africa due to favourable synoptic conditions (Knippertz et al., 2017). Note that we hereafter consider UTC time rather than Benin local time (UTC+1).

3.1 Observational data used

Two complementary and co-located instruments installed at Savè supersite were used to provide information on the LLSC macrophysical characteristics: a ceilometer for the cloud base height (CBH) and a cloud radar for the cloud top height (CTH).

30   Through the backscatter profiles measured by the ceilometer, manufacturer software automatically provides each minute three estimates of CBH allowing the detection of several cloudy layers. As we focus on the LLSC (the lowest cloudy layer), we use only the lowest value (thereafter CBHs). The CTHs are derived from 5-min averaged radar reflectivity vertical profiles by a methodology described in Babić et al. (2019) and Adler et al. (2019). According to Dione et al. (2019) the top

of the LLSC evolves overall under 1200 m a.g.l. To be consistent with this outcome, an upper limit of 1200 m a.g.l was applied to the CTHs. Unfortunately, several values of CTHs are missing particularly during daytime for many selected cases.

The meteorological conditions at the surface (temperature, relative humidity, and, pressure of the air at 2-m height), and, the different terms of the surface energy budget were continuously acquired. In this study, the net radiative flux (R_n), the
5   surface sensible (SHF) and the latent heat (LHF) fluxes measured at 4 meters above ground level (m a.g.l) are used. SHF and LHF are deduced from high-frequency (20 Hz) measurements processed with Eddy-covariance methods with the TK3.11 software (Mauder et al., 2013).

The thermodynamical and dynamical characteristics of the low troposphere are retrieved from the radiosoundings. A standard radiosonde was launched every day at 05:00 UTC and usually rose up to 20 km a.g.l. On IOP days, 3 additional
10   radiosondes were performed at 23:00 on day D, and at 11:00 and 17:00 UTC on day D+1. In between these soundings, so-called re-usable radiosondes were more frequently launched, at regular time interval in order to provide higher temporal resolution of the conditions within the ABL. The re-usable radiosondes reached a maximum height of around 1500 m a.g.l. During the six first IOPs of DACCIWA the frequent soundings were performed hourly and each 1.5 h during the others. The radiosondes data were smoothed by averaging with final vertical resolution of 10 m. Additionally, measurements of an ultra-
15   high frequency (UHF) wind profiler are used to derive the NLLJ core height at 15 min time interval (Dione et al., 2019).

3.2 Derived diagnostics to monitor the LLSC

We define some diagnostics to monitor the evolution of LLSC layer: the *fraction of the low cloud coverage*, the *LLSC base height* and *the homogeneity of the cloud layer*, the *link between the LLSC and the surface*, as well as *characteristic*
20   *times of the LLSC*. The LLSC depth would also be a key diagnostic, but the low availability of CTHs cloud radar-based estimates during daytime limits its monitoring. In addition to that, the humidity and temperature sensors onboard the radiosonde were affected by the water deposition during the crossing of the LLSC layer, so neither these are always reliable for the CTH estimate (Adler et al., 2019; Babić et al., 2019a).

The diagnostics are calculated over a time interval of 10 minutes with moving window of 5 minutes, which roughly
25   corresponds to the convective time scale. Figure 2 illustrates our methodology, with an example of the measurements and the derived diagnostics for the case of 26-27 July 2016.

- *Fraction of the low cloud coverage*: The low-cloud fraction (*CF*) is defined as the percentage of 1-min ceilometer CBHs lower than or equal to 1000 m a.g.l. Thus, *CF* greater or equal to 90% corresponds to the presence of LLSC. A similar methodology was used by Adler et al. (2019), but with a threshold of 600 m a.g.l. We extend the upper limit to 1000 m a.g.l
30   to take into account of the rising of the LLSC base during the convective phase (Lohou et al., 2020). On 27 July 2016 (Fig. 2), the few periods between 04:00 UTC and 11:30 UTC with CF < 90% indicate intermittent break within the LLSC deck. This feature is common to many other cases.
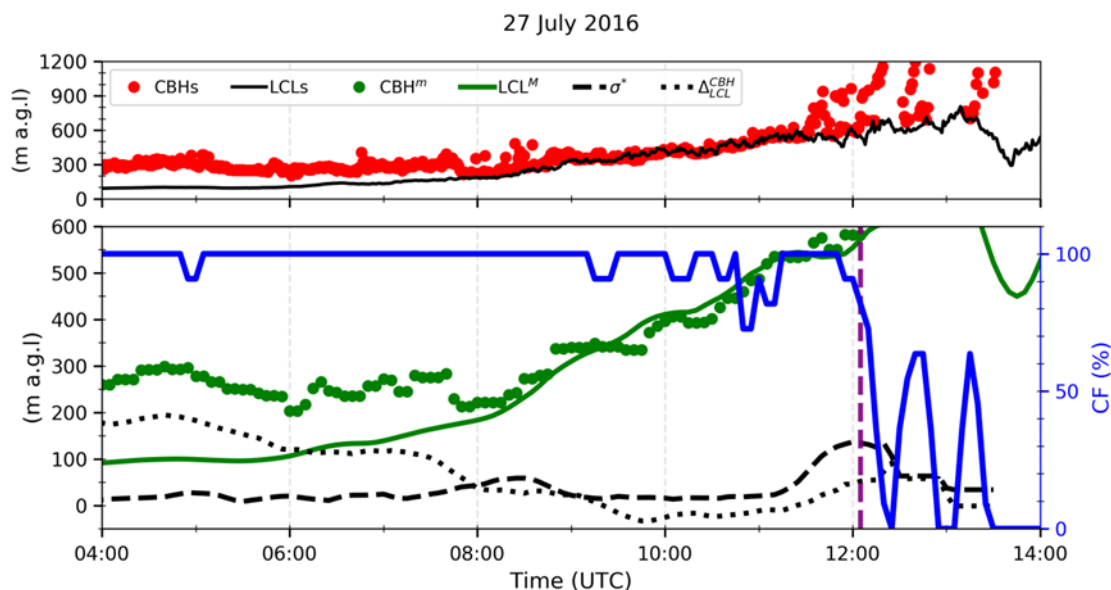
Figure 2 : Time series of, 1-min ceilometer-derived CBHs and surface-based lifting condensation level (LCLs) (upper panel), and derived 5-min diagnostics (lower panel), minimum of CBHs (CBH^m), mean LCLs (LCL^M, full green line), standard deviation of the difference between CBHs and CBH^m (σ^*, dashed black line), The difference between CBH^m et LCL^M (Δ_{LCL}^{CBH}, dotted black line) and LLSC coverage fraction (CF, full blue line), between 04:00 and 14:00 UTC on 27 July 2016. The vertical dashed purple line marks the breakup time of the LLSC layer (T_b).

- *LLSC base height and homogeneity of the cloud layer:* As seen in Fig. 2, the cloud "base height" may be more or less homogeneous in time and space, from a compact level cloud deck (like from 06:00 UTC to 06:30 UTC in Fig. 2) to a

5   fragmented Sc or even separated Cu clouds (like from 12:30 UTC to 13:00 UTC in Fig. 2). In the latter case, the ceilometer beam often hits Cu cloud base or higher edges introducing a large variability of the so-called and measured "CBH" (which is here more rigorously the first height above ground, with detected clouds). In order to take this aspect into account in the definition of the LLSC base, and to quantify the LLSC base homogeneity, we define two other diagnostics based on the 1-min ceilometer-derived CBHs. The first one is a characteristic LLSC cloud base height, defined as the minimum of CBHs

10   over the 10-min intervals (CBH^m). The second, is the standard deviation of CBHs (<=1000 m a.g.l) minus CBH^m within the 10-min intervals (σ^*), which gives an insight on the LLSC layer heterogeneity by deleting the effect of CBH morning increase. Small values of σ^* indicate nearly constant CBHs, that is horizontally homogenous base in the cloud layer (like from 04:00 UTC to 06:30 UTC on 27 July). High values of σ^* indicate irregular bases of the stratus layer or a mix of cloud base and edges after the stratus breakup (like from 12:30 UTC to 13:00 UTC on 27 July). The increase of σ^* from 21 to 135

15   m after 11:00 UTC on 27 July (Fig. 2), typically indicates an evolution towards a more heterogeneous LLSC layer.

- *Link between the LLSC and the surface:* When a stratiform cloud is coupled to the surface, its base coincides rather well with the LCL (Wood, 2012; Zhu et al., 2001). So that, the coupling between the LLSC and the surface may be assessed by the distance between the LCL and the cloud base height. We define LCL^M as the mean value of LCL calculated on 10-min

time interval by the use of Romps (2017) formulation with near surface meteorological measurements. The coupling is estimated by $\Delta_{LCL}^{CBH} = CBH^m - LCL^M$. On 27 July 2016 (Fig. 2), Δ_{LCL}^{CBH} is initially around 190 m, from 04:00 to 06:00 UTC indicating that the LLSC is decoupled from the surface. The progressive increase of the LCL starting around 06:00 UTC leads to the coupling of the LLSC with the surface slightly before 08:00 UTC.

5 Finally, the diagnostics LCL^M, Δ_{LCL}^{CBH} and σ^* defined before are smoothed with a moving average over 30 minutes every 5 min (Fig. 2).

- *Characteristic times of the LLSC*: From the above diagnostics, two specific times characterizing the LLSC lifetime are determined.

• The surface-convection influence time (T_i) corresponding to the time from which the low-level cloud coverage

10 reacts to solar heating at the surface. The method to determine T_i depends on the evolution of LLSC during the

convective phase. Thus, it will be precisely defined later in the text, after the presentation of the different observed

scenarios.

• The breakup time of the LLSC (T_b) which corresponds to the end of the LLSC occurrence. It is the time (after 06:30

UTC) from which *CF* is lower than 90% during at least one hour. Figure 2 (lower panel) shows several periods,

15 between 09:00 UTC and 11:00 UTC, with *CF* lower than 90%, but for less than one hour, so that they are included in

the LLSC lifetime. For this case, T_b is at 12:05 UTC.

3.1 LWP budget

The equation of LWP tendency is based on the assumption of an horizontally-homogeneous stratocumulus, vertically

20 well-mixed, by the convective turbulence driven by the cloud-top cooling (van der Dussen et al., 2014, 2016; Wood, 2012). Following van der Dussen et al. (2014) the LWP tendency can be split into five relevant processes:

$$\frac{\partial \text{LWP}}{\partial t} = \text{BASE} + \text{ENT} + \text{PREC} + \text{RAD} + \text{SUBS} \tag{1}$$

in which

$$\text{BASE} = \rho\eta(\overline{w'q_t'}^b - \Pi\gamma\overline{w'\theta_l'}^b) \tag{1.a}$$

$$\text{ENT} = \rho w_e(\eta\Delta q_t - \Pi\gamma\eta\Delta\theta_l - D\Gamma_{ql}) \tag{1.b}$$

$$\text{PREC} = \rho\Delta P \tag{1.c}$$

$$\text{RAD} = \rho\eta\gamma\Delta F_{rad} \tag{1.d}$$

$$\text{SUBS} = -\rho D\Gamma_{ql}w_{s,h} \tag{1.e}$$

representing the effects of turbulent moisture and heat fluxes at the cloud base (BASE), evaporation or condensation caused by entrainment of ambient air from aloft (ENT), precipitation formation (PREC), radiative cooling (RAD) and large-scale subsidence (SUBS) at the cloud top.

In the above equations (1.a) to (1.e), $\overline{w'q_t'}^b$ and $\overline{w'\theta_l'}^b$ are respectively the total moisture (q_t) and liquid-water potential temperature (θ_l) heat fluxes at cloud base (superscript "b"), ρ is the mean air density over the cloud layer, D is the cloud depth. ΔF_{rad} and ΔP are the differences, in net radiation and precipitation respectively, between the cloud top and base (van der Dussen et al., 2014). $\Delta \theta_l$ and Δq_t are the jumps of respectively θ_l and q_t across the cloud top. w_e is the entrainment velocity.

The equations also introduce the following parameters: The Exner function $\Pi = \left(\frac{P}{1000}\right)^{\frac{R_d}{C_p}}$; the adiabatic lapse rate of liquid water content $\Gamma_{ql} = g\eta(\frac{q_s}{R_d\overline{T}} - \frac{\gamma}{C_p})$; $\gamma = \frac{L_v q_s}{R_v \overline{T}^2}$ and $\eta = \left(1 + \frac{L_v\gamma}{C_p}\right)^{-1}$. In those parameters, P and $\overline{T}$ are respectively the pressure and temperature of the Sc layer, q_s is the saturation water vapour specific humidity at P and $\overline{T}$. R_d and R_v are respectively the dry air and water vapour gas constant, L_v is the vaporization latent heat of water, C_p the specific heat of dry air at constant pressure, and g is the gravitational acceleration.

For our analysis of a set of DACCIWA cases, we consider the LWP budget in early morning, and use the 05:00 UTC radiosounding, the ceilometer and the cloud radar measurements to estimate some of the terms of equation (1). This is the optimized time for the assumption of horizontally homogeneous cloud. The term PREC is supposed to be close to zero because no significant rain was measured at surface for the selected cases. The BASE term is not estimated because the turbulent fluxes at its base cannot be deduced from the available data set at Savè supersite. According to Pedruzo-Bagazgoitia et al. (2020), this term is small at this time relatively to the radiation, entrainment and subsidence terms RAD, ENT and SUBS. The latter are the most significant contributions in early morning that we attempt to estimate, based on further hypotheses.

For the estimate of RAD (Eq. 1.d), shortwave radiation is zero at that time, and ΔF_{rad} estimation is only based on the longwave radiation. Typically, the longwave radiative cooling is overall confined over about ten meters in the upper part of the well-mixed stratocumulus layer (Pedruzo-Bagazgoitia et al., 2020; Wood, 2012). This cooling occurs because the cloud top droplets emit more infrared radiation towards the free troposphere than they receive from the drier air above. In nighttime conditions, the longwave cooling at cloud top is thus related to the difference in temperature across the cloud top, and to the difference of emissivity between cloudy and dry air (resp. ε_c and ε_a) aloft. ε_a depends on the air temperature and moisture, whereas ε_c is strongly influenced by the cloud LWP. On this basis, we deduce ΔF_{rad} from the cloud-top radiative cooling (RadF), approximated with use of the Stephan-Boltzmann's law:

$$\rho C_p \Delta F_{rad} = RadF \approx \sigma(\varepsilon_c(T^+ - \Pi\Delta\theta_l)^4 - \varepsilon_a(T^+)^4) \qquad (2)$$

where $\sigma = 5.67 \times 10^{-8}$ W m^{-2} is the Stephan-Boltzmann's constant, T^+ is the state temperature of clear air just above the cloud top and $\Pi\Delta\theta_l$ represents the state temperature difference along the inversion layer. Note that RadF is positive for a cooling.

This formulation assumes that the above ambient air absorbs completely the radiation from potential mid-level and high-level cloud layers and irradiates at temperature T^+. In the infrared band, the stratocumulus behaves nearly like an ideal blackbody (Liu et al., 2018), therefore, we consider $\varepsilon_c = 1$ in this study. While, ε_a is retrieved by using the formulation of Prata (1996):

$$\varepsilon_a = 1 - (1 + c_1 \text{IWV}) * e^{-\sqrt{c_2 + c_3 \text{IWV}}} \tag{3}$$

5 with $c_1 = 0.1 \text{ m}^2 \text{ kg}^{-1}$, $c_2 = 1.2$, $c_1 = 0.3 \text{ m}^2 \text{ kg}^{-1}$ and IWV, the Integrated Water Vapour above the cloud layer. IWV is calculated by using the sounding measurements with CTH as lower limit of the atmosphere.

For the term ENT (Eq. 1.b), we use the parameterization of Stevens et al. (2005) to estimate the entrainment rate (w_e):

$$w_e = A * \frac{\Delta F_{\text{rad}}}{\Delta \theta_l} \tag{4}$$

in which A is a non-dimensional quantity representing the efficiency of the warming caused by the input of warmer ambient air from aloft into the cloud layer by the convective eddies generated by cloud-top radiative cooling. A depends on Δq_t, wind
10 shear through the inversion, surface turbulent fluxes and cloud microphysical processes via the buoyancy flux vertical profile (van der Dussen et al., 2014; Stevens et al., 2005). Therefore, it has a spatio-temporal variability (Stevens, 2006). Nevertheless, its value is generally fixed and treated as a constant parameter in several research studies (e.g. van der Dussen et al., 2014; vanZanten et al., 1999). The used value of A found in the literature varies from one study to another. By considering the results of the LES made by Pedruzo-Bagazgoitia et al. (2020) on a DACCIWA case, just before sunrise, with
15 $w_e \approx 4.5 \text{ mm.s}^{-1}$, $\Delta \theta_l \approx 4 \text{ K}$ and RadF $\approx 43 \text{ W.m}^{-2}$, and considering $\rho \approx 1.13 \text{ kg.m}^{-2}$ as the average value from the surface to 1000 m above (from 26 June 05:00 UTC sounding), we obtain $A \approx 0.5$. This means that the contribution of entrainment driven by convective turbulence in the heat budget at the cloud top is around 2 times smaller than that driven by the cloud-top radiative cooling. For simplicity, and in lack of more precised estimates, we assume here the same behaviour for all the DACCIWA cases, and consider $A = 0.5$ in our analysis.

20 The jumps in temperature $\Delta \theta_l$ and in total water content Δq_t are estimated based on the radiosoundings. We write $\theta_l = \theta - \frac{1}{\Pi} \left(\frac{L_v}{C_p} \right) q_l$, with θ as the potential temperature, whereas $q_t = q + q_l$. We define:

$$\Delta \varphi \approx \varphi^+ - \varphi^- \tag{5}$$

where φ can be either θ_l or q_t. φ^+ and φ^- are the values of the variable φ just above and just below the cloud top respectively. Under the assumption of a well-mixed cloud layer, θ_l (q_t) is conserved from the surface up to the cloud top and increases (decreases) abruptly in the warmer (drier) ambient air right above (vanZanten et al., 1999). Thus, $\Delta \theta_l$ and Δq_t can
25 be estimated from the vertical profiles of θ and q derived from the morning standard sounding measurements. For θ_l^+ and q_t^+, we consider the mean over the 50 m above CTH. For θ_l^- and q_t^-, we consider the mean over the 50 m below the CBH. This is based on the conservation of those variables through the cloud, and the fact that we have no measurement of liquid water content with the radiosoundings. In sum, we use $q_t^- = q_{t \text{ \{below cloud top\}}} = q_{t \text{ \{below cloud base\}}} = q_{\text{ \{below cloud base\}}}$ and $\theta_l^- = \theta_{l \text{ \{below cloud top\}}} = \theta_{l \text{ \{below cloud base\}}} = \theta_{\text{ \{below cloud base\}}}$.

For the term SUBS (Eq. 1.e), we have no possibility of estimating precisely the large scale subsidence at the cloud top. But in order to have an approximation of its magnitude at the end of the stratus phase, we may consider that the cloud top is stationary, like in Pedruzo-Bagazgoitia et al. (2020). According to the cloud radar CTH estimates, this hypothesis if often met during DACCIWA cases at this time of the day, as also observed by previous analyses of the DACCIWA dataset (Adler

5   et al., 2019; Babić et al., 2019a; Dione et al., 2019). But the availability of CTH estimates is not large enough to assess the cloud top evolution for all cases. Based on the stationarity of the cloud top at the time of our LWP budget analysis, the term SUBS is estimated with the assumption that $\frac{\partial h}{\partial t} = w_{s,h} + w_e \approx 0$ (Lilly, 1968).

4 LLSC during the stratus phase

10   In this section, we start by documenting the stratus phase, especially its end. The aim is to analyse the way the LLSC is coupled to the surface and if that implies different cloud characteristics (macrophysical properties and LWP terms) just before the convective phase. During the DACCIWA campaign field, the sunrise occurred at Savè between 05:33 and 05:42 UTC (Kalthoff et al., 2018). According to Lohou et al. (2020), the final convective phase starts between 07:30 and 09:00 UTC. The last radiosonde launched before the convective phase is performed at 06:30 UTC, consequently, the analysis in

15   this section concerns the period from the beginning of the stratus phase to 06:30 UTC on Day-D+1.

4.1 Coupled and decoupled LLSC

We first consider the start of the stratus phase and define the CBH of the LLSC by the median value of 1-min CBHs over the firsts 15 minutes. When the LLSC forms, its base is located around the NLLJ core height, where the cooling driven by

20   the horizontal advection is optimal (Adler et al., 2019; Dione et al., 2019; Lohou et al., 2020). This is visible in Fig. 3a, which shows CBH as a function of the 15-min NLLJ heights median value over one hour centered on the stratus phase start. The averaged LLSC base ranges from 50 to 500 m a.g.l, similarly to the averaged NLLJ core height. Figure 3b shows that meanwhile, and except for one case among the 22 selected cases, CBH is a hundred meters above the mean surface-based LCL over the corresponding time interval. This means that the LLSC is decoupled from the surface when it forms.
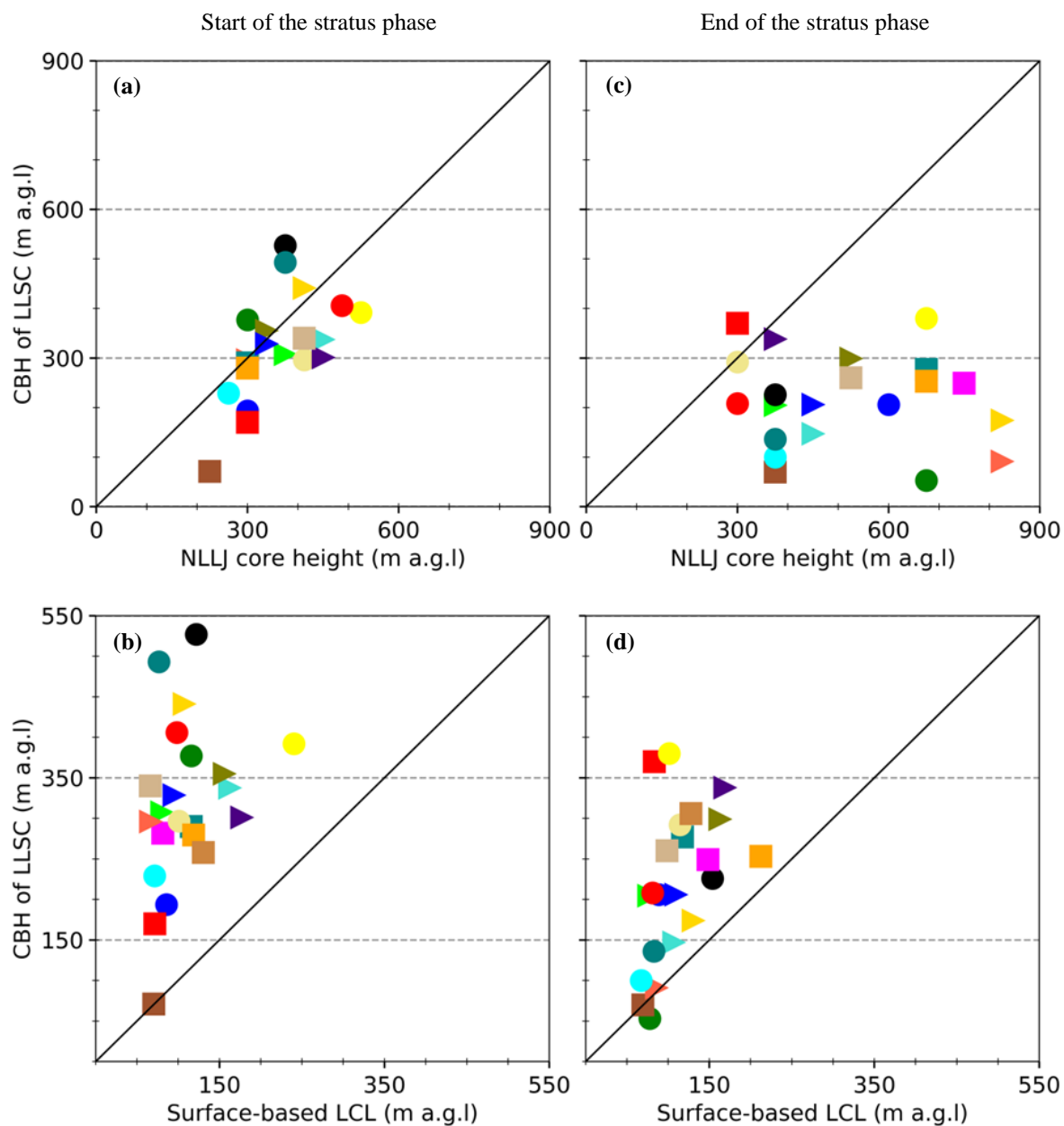
Figure 3 : CBH of LLSC against the NLLJ core height (top panels), the surface-based LCL (bottom panels), at the start **(a, b)** and at the end of stratus phase **(c, d)**. Each of the 22 selected cases is represented by a different marker. (See the text for precise definition)
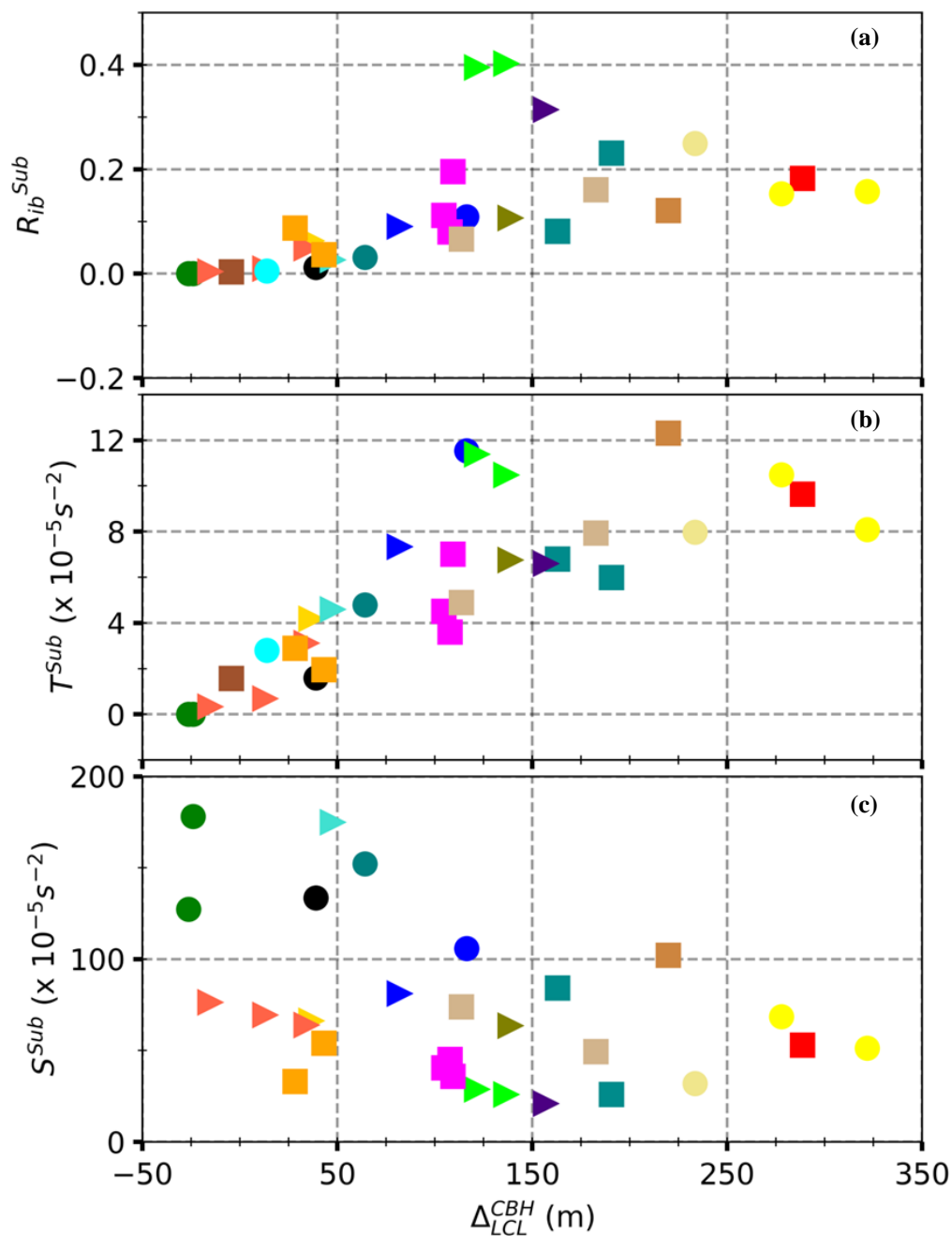
Figure 4 : (a) R_{ib}^{Sub}, (b) T^{Sub} and (c) S^{Sub} as a function of Δ_{LCL}^{CBH}, performed by using all radiosoundings available from 04:00 to 06:30 UTC on each studied case. Each marker corresponds to one case.

Now we consider the end of the stratus phase, and, CBH of LLSC and surface-based LCL are the medians of respectively CBH^m and LCL^M between 04:00 and 06:30 UTC, the same for the NLLJ core height. One can see that the relationship between CBH and the NLLJ core height has totally changed (Fig. 3c). There is no clear linear link between both and CBH remains lower than 300 m a.g.l in average. This is most likely because, during the stratus phase, the jet axis is shifted upward

5   by the turbulence within the LLSC layer (Adler et al., 2019; Dione et al., 2019; Lohou et al., 2020). For most of the cases, the averaged CBH has decreased by the end of the stratus phase (Fig. 3b and d). In some cases, CBH coincides pretty well with LCL (Fig. 3d), indicating a coupling between the LLSC and the surface. But, in others, CBH is still at least 100 m higher than LCL, meaning that the LLSC remains decoupled from the surface.

This different nature of coupling between the cloud and the surface is further analyzed by using the bulk Richardson

10   number (Stull, 1988) of the subcloud layer (R_{ib}^{Sub}). It reads:

$$R_{ib}^{Sub} = \frac{T^{Sub}}{S^{Sub}} \text{ with } T^{Sub} = \frac{g}{\theta} * \frac{\delta\theta}{CBH} \text{ and } S^{Sub} = \left(\frac{\delta U}{CBH}\right)^2. \tag{6}$$

T^{Sub} and S^{Sub} are respectively the thermal and vertical wind shear contributions to the Richardson number. $\frac{\delta\theta}{CBH}$ and $\frac{\delta U}{CBH}$ are the vertical gradient of θ and horizontal wind speed (U) respectively, within the subcloud layer (between the cloud base and the surface), with the assumption that U is null at surface. R_{ib}^{Sub} is estimated with all radiosoundings available from 04:00 to 06:30 UTC, for each studied case. For this, the median of CBH^m over the 30 minutes centered on the radiosounding time is

15   used (in Eq. 6).

Figure 4 shows R_{ib}^{Sub} (Fig. 4a), T^{Sub} (Fig. 4b) and S^{Sub} (Fig. 4c) as a function of Δ_{LCL}^{CBH} (the median over 30 minutes centered on the radiosounding time for this plot). Smaller Δ_{LCL}^{CBH} are associated with lower R_{ib}^{Sub}. Interestingly, for Δ_{LCL}^{CBH} smaller than or equal to 75 m, R_{ib}^{Sub} are about of less than or equal to 0.1, and vice-versa (Fig. 4a). This supposes that, the potential early morning coupling between the LLSC and the surface is driven by the underlying shear-driven turbulent mixing. A

20   similar tendency was found by Adler et al. (2019) when analyzing the soundings performed along the stratus phase of 11 IOPs, and explained by the role of shear-related processes in the formation of the LLSC when the LCL is close to the CBH, that is when the surface is coupled to the cloud.

However, while T^{Sub} has a quite similar relationship than R_{ib}^{Sub} with Δ_{LCL}^{CBH}, it is not the case for S^{Sub}. For CBH close to the LCL, although the subcloud layer is well mixed, the shear-driven turbulence in the subcloud layer is not necessarily larger.

25   Thus, the nature of coupling between the LLSC and the surface seems to be mostly linked to the thermal stratification in the subcloud layer, rather than to the shear. This outlines the relative importance of the cloud-top cooling in the production of turbulent mixing in the subcloud layer which couples the LLSC to the surface.

Based on the Fig. 4 (a and b), the value of 75 m is used thereafter as a threshold for Δ_{LCL}^{CBH} to distinguish the coupling nature at the end of the stratus phase. Through this classification, our set of 22 studied cases includes 9 cases in which the

30   LLSC layer is coupled to the surface (case C) and then decoupled (case D) for the 13 others cases (Table A-1). Among the cases C, 3 are IOPs (N° 5, 6 and 8).
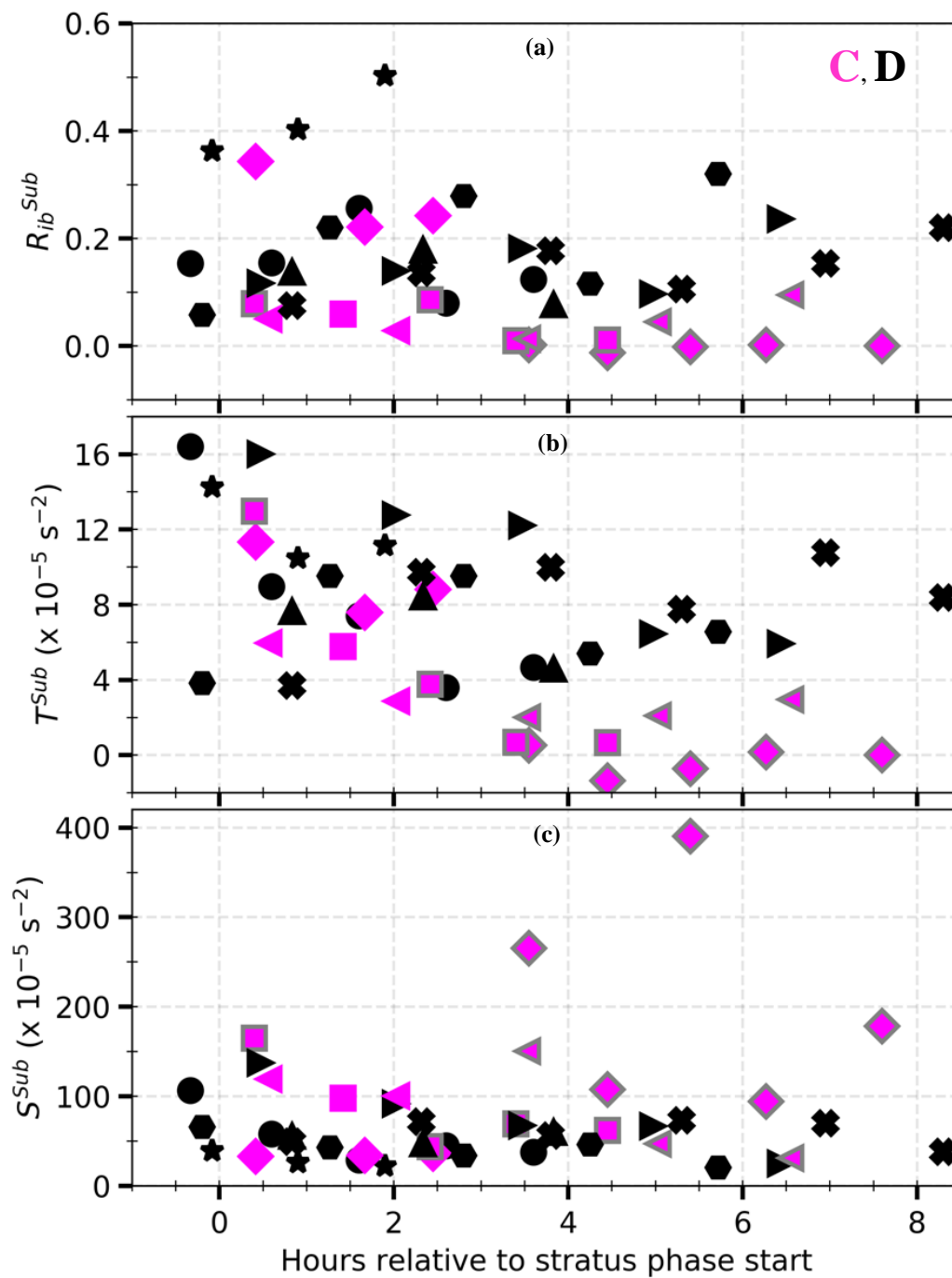
Figure 5 : **(a)** R_{ib}^{Sub}, **(b)** T^{Sub} and **(c)** S^{Sub}, performed by using all the soundings available during the stratus phase on the 9 IOPs (Table A-1). The quantities are presented against the sounding time which is expressed in hours relative to the start of the stratus phase. Each IOP is represented by a marker. C and D stand for the coupled and decoupled cases respectively. The grey edge indicates that $\Delta_{LCL}^{CBH} \leq 75$ m at the sounding time.

We have seen before that, for almost all the cases, the LLSC is decoupled from the surface at the start of the stratus phase. The lowering of the LLSC base was first pointed out by Babić et al. (2019a) for the 07-08 July study case. We now try to understand why the LLSC may couple to the surface by the end of the stratus phase only in some cases.

Based on the re-usable radiosoundings available for the 9 IOPs, the temporal evolution of R_{ib}^{Sub} and its composing terms have been calculated from the start of the stratus phase up to 06:30 UTC (Figure 5). R_{ib}^{Sub}, T^{Sub} and S^{Sub} in cases C and D are similar when the stratus phase begins. For cases C, T^{Sub} decreases within the three following hours while S^{Sub} remains almost constant, which cause a decrease of R_{ib}^{Sub} (Fig. 5a and b). A few cases D show a slightly similar pattern, but only for a much shorter time. In cases C presented in Fig. 5, the steady coupling with the surface occurs within 2-4 hours after the beginning of the stratus phase. The same behaviour is observed for the cases C which are not IOP and therefore not included in Fig. 5 (not shown). Furthermore, for two out of three cases C in Fig. 5, one can note an increase of S^{sub} but only after the coupling. Considering these results, it appears that the turbulence below the LLSC base, either dynamic or thermal, may not be the main driver of the coupling in the cases C.

The numerical experiments performed by Dearden et al. (2018), based on the LLSC occurrence of 04-05 July at Savè supersite (case D, IOP 7), showed that the lowering of the LLSC may be due to cloud droplets sedimentation. Furthermore, the occurrence of the cases C and D over the DACCIWA field campaign (Table A-1) suggests that the coupling between the LLSC and the surface is sensitive to the synoptic scale atmospheric circulation within the low-troposphere. Indeed, all the cases C, except one, occurred between the 26 June and 8 July 2016, the first days of the post-onset phase characterized by a well-established and undisturbed monsoon flow over studied area (Knippertz et al., 2017).

The turbulent mixing below the LLSC is not the principal driver of the coupling between the cloud and the surface. But this turbulence has a crucial role for the maintenance of this coupling during the remaining time of the stratus phase, as indicated by the reduction of thermal stability in the subcloud layer (Fig. 5b). Indeed, the contributions of shear-driven turbulence below the NLLJ and turbulence due to the cooling at the cloud top are important for mixing potential temperature in the subcloud layer (Dione et al., 2019; Lohou et al., 2020). In the LES experiment under windless conditions carried out by Pedruzo-Bagazgoitia et al. (2020), the radiative cooling at cloud top was the unique source of turbulence in the ABL until sunrise, and the coupling between the cloud and the surface was maintained.

In conclusion, the LLSC forms typically decoupled from the surface. Subsequently, its base lowers during the first hours of the stratus phase. In the cases C (9 cases out of 22), this decrease is more important, leading to the coupling between the cloud and the surface before the sunrise. In the following, we analyze the LLSC characteristics in the C and D cases at the end of the stratus phase.
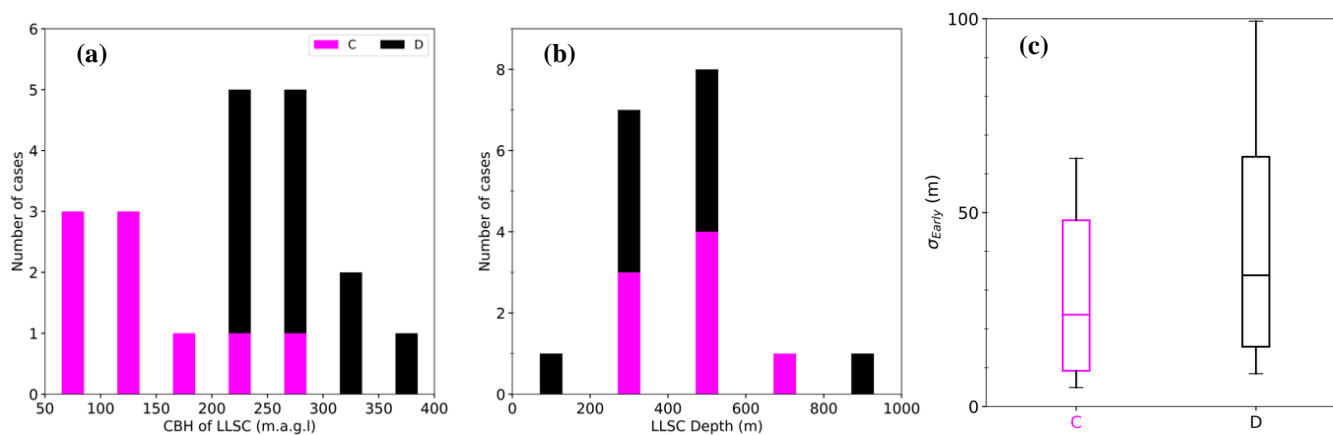
Figure 6 : Statistic on the LLSC macrophysical characteristics at the end of the stratus phase, performed on the 20 cases (the 9 C and 11 D out of 13), for which the LLSC is present (CF ≥ 90%) over at least 70% of the time. **(a)** Distribution of LLSC CBH, the same than on Figure 3. **(b)** Distribution of the LLSC depth calculated by using the median value of CTHs between 04:00 and 06:30 UTC as the LLSC summit. The depth was not estimated for 2 cases (1 C and 1 D) among the 20 due to CTHs missing data. **(c)** Statistical information on σ_{Early}, which is the median value of σ^* between 04:00 and 06:30 UTC. The edges of each box represent the 25th (bottom) and 75th (top) percentiles and the whiskers the minimum, the median and maximum values from the bottom to the top respectively. C and D stand for the coupled and decoupled cases respectively.

The distributions of averaged LLSC CBH and depth at the end of the stratus phase are shown on Fig. 6a and b respectively. Only the 20 cases for which the cloud is persistent (CF ≥ 90%) over at least 70% of the time are considered

5 (including 9 cases C and 11 cases D). Note that, the depth could not be estimated for 2 cases because of CTH missing data. The CBH ranges within 50-200 m a.g.l for cases C, and within 200-400 m a.g.l for cases D. This clear difference between coupled and decoupled LLSC explains the bimodal distribution of morning CBH found by Kalthoff et al. (2018). It is explained by the fact that the base of the cloud descends during the stratus phase in cases C. In contrast, the morning LLSC depth does not depend on the state of the coupling with the surface.

10 Figure 6c presents the statistical information of σ_{Early}, which is the median value of σ^* between 04:00 and 06:30 UTC for the considered cases. The median of σ_{Early} is 24 m for cases C and 34 m for the cases D. Their 25th percentiles and minimums are close, but, the 75th percentile for cases D is more than 10 meters higher than that of cases C, and the maximum is significantly larger, close to 100 m. This reveals the larger LLSC base heterogeneity found for several cases D. Likely, the coupling with the surface limits the fragmentation of the LLSC layer, and helps maintaining the homogeneity of the cloud in

15 cases C.

In brief, the mechanism of coupling favours lower CBH and slightly more homogeneous cloud base in the cases C. But the LLSC depth is similar in cases C and D, so that the LLSC vertical extension is not influenced by the coupling with the surface. This may be related to the negligible contribution of surface fluxes during the night.
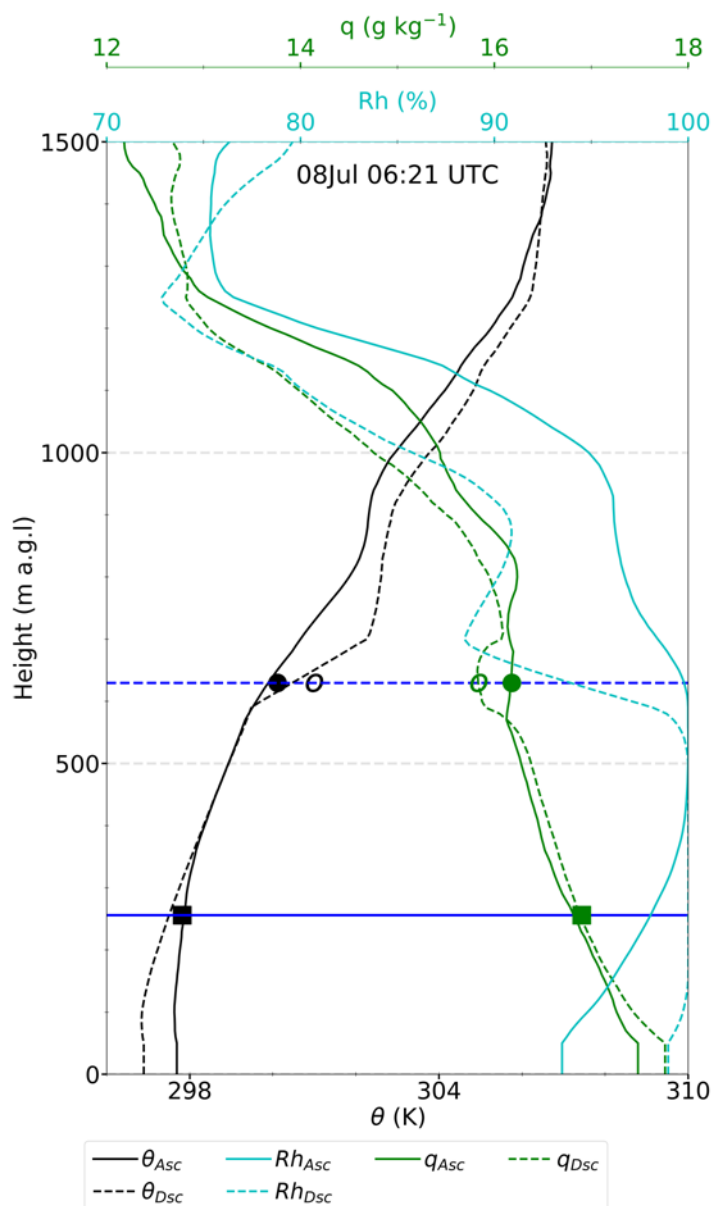
Figure 7 : Vertical profiles of the low-troposphere acquired by the re-usable radiosonde of 08 July 2016 at 06:21 UTC, when the probe ascents ('Asc', filled line) and descends ('Dsc', dashed line). The variables shown are the relative humidity (Rh), the potential temperature (θ) and the water vapour specific humidity (q). The horizontal blue lines mark the CBH (filled line) from the ceilometer, and the CTH (dashed line) from the cloud radar. The values of φ^{+}(φ^{-}) (section 3.1) for θ and q are marked with dot (square). The filled symbols correspond to the ascent, whereas the unfilled symbols correspond to the descent.

4.2 LWP terms

In order to deepen the analysis, we make an attempt to estimate the LWP terms at the end of the stratus phase, i.e. just before the convective phase. Several questions motivate this attempt:

5   1) Do we find similar results with observations as with previous numerical simulations, particularly that of Pedruzo-Bagazgoitia et al. (2020)?

2) Does the LWP budget analysis help us to depart the cases C and D?

As seen previously, the most important contributions in the LWP budget are that of radiation, entrainment and subsidence. Based on the available observations, we estimate RAD and ENT, and also give a rough order of magnitude of SUBS. We

10   first discuss the jumps Δq_t and $\Delta\theta_l$ across the cloud top, which are involved in ENT and RAD terms. They are estimated by use of the radiosoundings, although the crossing of the wet cloud makes it delicate.

Indeed, the crossing of the cloud wets the probe, such that the measurements get possibly erroneous at the exit of the cloud. In order to evaluate the impact of this issue on our jump estimations from the 05:00 UTC standard radiosonde, we first consider a re-usable sounding at a different time, for which the probe has crossed the cloud both at ascent and descent.

15   At ascent, the sensor is reliable at cloud base, but may get wrong data when it reaches cloud top. At descent, it is the reverse: correct at cloud top but possibly erroneous measurements when it reaches cloud base. This is shown in Fig. 7 which displays the θ, q and relative humidity (Rh) measured by the re-usable sounding of 08 July 2016 at 06:21 UTC, during both the ascent and the descent of the probe. By analyzing Rh vertical profiles, one can see that the upper limit of the saturated layer (Rh >= 98.5), i.e. LLSC layer top, obtained by the descent measurements is more consistent with the cloud radar-estimated CTH

20   than that obtained during the ascent. Further, the descent measurement indicates warmer and drier atmospheric conditions from the CTH to around 500 meters above, with θ^+ (q^+) around 1 K (0.3 g kg^{-1}) higher (smaller). Analysing all re-usable soundings of that kind during daytime, we find that the maximum underestimation (overestimation) of θ^+ (q^+) during the ascent due to the wetting of the sensors is of about 1.2 K (0.3 g kg^{-1}). The overestimation of q^+ by the ascending sounding is within the measurement accuracy. While, compared to the 0.2° C measurement accuracy, the underestimation of θ^+ is

25   significant. Consequently, we only consider a systematic error of 1.2 K on the estimates of θ^+ from the 05:00 UTC standard radiosounding, for which we can only rely on the ascent (the descent is too far away from the area).

Figure 8 displays Δq_t and $\Delta\theta_l$ against q^- and θ^- respectively, as estimated for the 14 cases (8 cases C and 6 cases D) among the 20 cases of Figure 6, for which there is evidence that the radiosonde flew throughout the LLSC layer. It first reveals that the thermodynamic conditions of the subcloud layer are quite steady during this summer period, with only 1.5

30   g kg^{-1} and 2 K variation range for humidity and temperature, respectively, over all the cases. Similar conclusion was found by Adler et al. (2019).
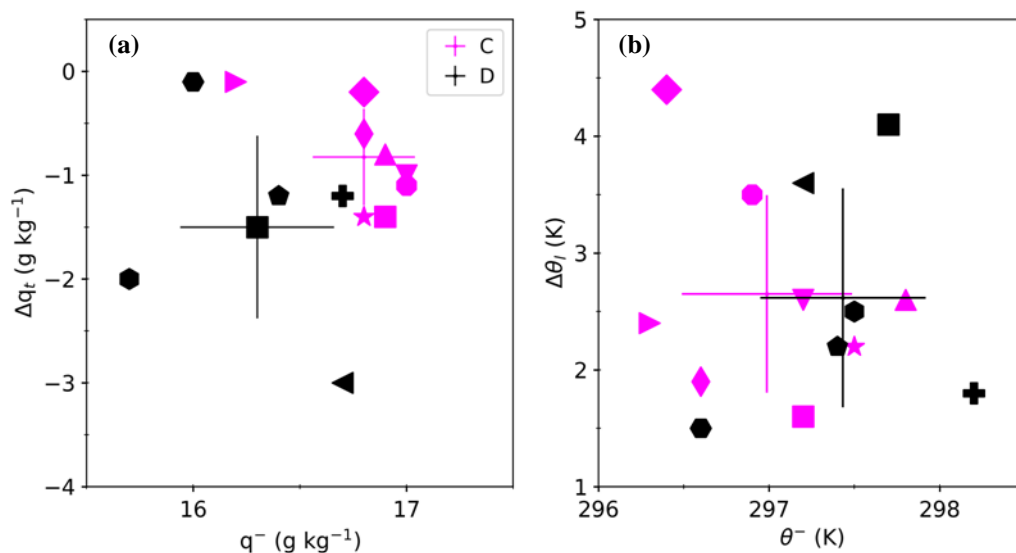
Figure 8 : Δq_t against q^- (**a**), $\Delta \theta_l$ against θ^- (**b**), derived from the 14 standard morning soundings for which the probe flew within the LLSC layer (Table A-1). In each panel, the error bars correspond to the standard deviation, and cross at the mean over all C (magenta) or D (black) cases. Each symbol represents a single LLSC case.

In the cases C, q^- ranges within the interval 16-17 g kg^{-1}, with a mean of 16.8 g kg^{-1} and a standard deviation of 0.5 g kg^{-1}. It is lower in the cases D, with an average of 16.3 g kg^{-1} and a standard deviation of 0.9 g kg^{-1}. Thus, in early morning, the air just below the LLSC is in average 0.5 g kg^{-1} moister in the cases C. This is qualitatively true for the entire stratus phase, when analyzing the re-usable soundings of the 9 IOPs (not shown). Δq_t is overall in absolute lower than 3.0 g kg^{-1}. It is

5   smaller than 1.5 g kg^{-1} for 85% of the cases. This indicates a generally weak moisture jump across the LLSC top. This is still more pronounced in the cases C, for which Δq_t remains lower than 1.5 g kg^{-1} in absolute.

The parameter θ^- ranges within 296-299 K. Beyond the same variability found in cases C and D, θ^- is in average around 0.5 K cooler in the cases C, probably because of the cloud base lowering. $\Delta \theta_l$, which varies within the interval 1-5 K, does not exhibit a clear difference between the cases C and D. Thus, the fact that the LLSC base gets closer to the surface in the

10   cases C does not impact the temperature jump across the LLSC top.

The magnitude of $\Delta \theta_l$ and Δq_t observed here in SWA conditions are much smaller than those typically found for the mid-latitude stratocumulus, which can be as strong as 10 K and -10 g kg^{-1} (van der Dussen et al., 2016; Duynkerke et al., 2004; Ghonima et al., 2016; Wood, 2012), especially over the ocean. The vertical profile used by Pedruzo-Bagazgoitia et al. (2019) to initialize their LES had a $\Delta \theta_l$ of 4.5 K and no humidity jump across the LLSC layer. This representation is consistent with

15   what we find for the moisture jump, but is on the sidelines for the temperature jump.

Table 1 : Median and standard deviation of some of the parameters in the RAD, ENT and SUBS formulation estimated from the 14 soundings presented on Figure 8. The standard deviation (in brackets) over the cases is not indicated when it is negligible. Our results are compared with the values used in van der Dussen et al. (2014).

Parameters	Order of magnitude	
	DACCIWA cases	Study case of van der Dussen et al. (2014)
$\overline{T}$	294 (0.7) K	283 K
$\overline{q}$	16.2 (0.6) g kg^{-1}	8.2 g kg^{-1}
RadF	40 (5) W m^{-2}	48 W m^{-2}
γ	~1.012 g kg^{-1} K^{-1}	0.55 g kg^{-1} K^{-1}
η	~ 0.28	0.42
Γ_{ql}	~ -2.28 g kg^{-1} km^{-1}	-1.86 g kg^{-1} km^{-1}
w_e	7.68 (2.8) mm s^{-1}	--

Table 1 compares our estimates of some parameters involved in the formulation of the RAD, ENT and SUBS terms with those of van der Dussen et al. (2014) study case. The quantities γ, η, and Γ_{ql} differ from the typical values used by these authors because the cloud layer is in average 11 K warmer and 8 g kg^{-1} wetter in our case. For these three parameters, the

10 standard deviation over the 14 cases is lower than 3% of the median. The median and the standard deviation of RadF are respectively about of 40 and 5 W m^{-2}. Our estimate of RadF, of 40 W m^{-2}, is in good agreement with the value of 43 W m^{-2} given by the Pedruzo-Bagazgoitia et al. (2020) simulations just before the sunrise. This is much smaller than the values of 50-90 W m^{-2}, typically found in the subtropical stratocumulus (van der Dussen et al., 2014; Wood, 2012). Given that the LLSC is warmer, we attribute this difference to the weaker temperature and nearly absent moisture jumps at its top.

15 We find only 5 W m^{-2} standard deviation for RadF, showing again that the conditions during this period remain surprisingly steady from one day to the other. Note that uncertainties of 0.2 K on T^{+}and 0.4 K on $\Delta\theta_l$ give a systematic error of around 2.2 W m^{-2} on RadF. Increasing systematically θ^{+} by 1.2 K for the temperature correction decreases RadF by about 6 W m^{-2}, which remains small.

The entrainment velocity, w_e, deduced from the parameterization of Eq. (4) has a median of 7.68 mm s^{-1} and its variability

20 is around 40% of the median. This is around 40% higher than the velocity obtained by Pedruzo-Bagazgoitia et al. (2020) with LES and among the highest values found by other authors (Duynkerke et al., 2004; Faloona et al., 2005; Ghonima et al., 2016; Mechem et al., 2010). Finally, this discussion shows that our estimates of RAD and ENT should be suitable, beyond the potential errors on entrainment efficiency (A). As mentioned in section 3.1, we only roughly approximate SUBS with the

assumption that $w_{s,h} = -w_e$ (stationary cloud top at the time of the sounding). This term has to be taken with more caution than the two other terms, due to this hypothesis.
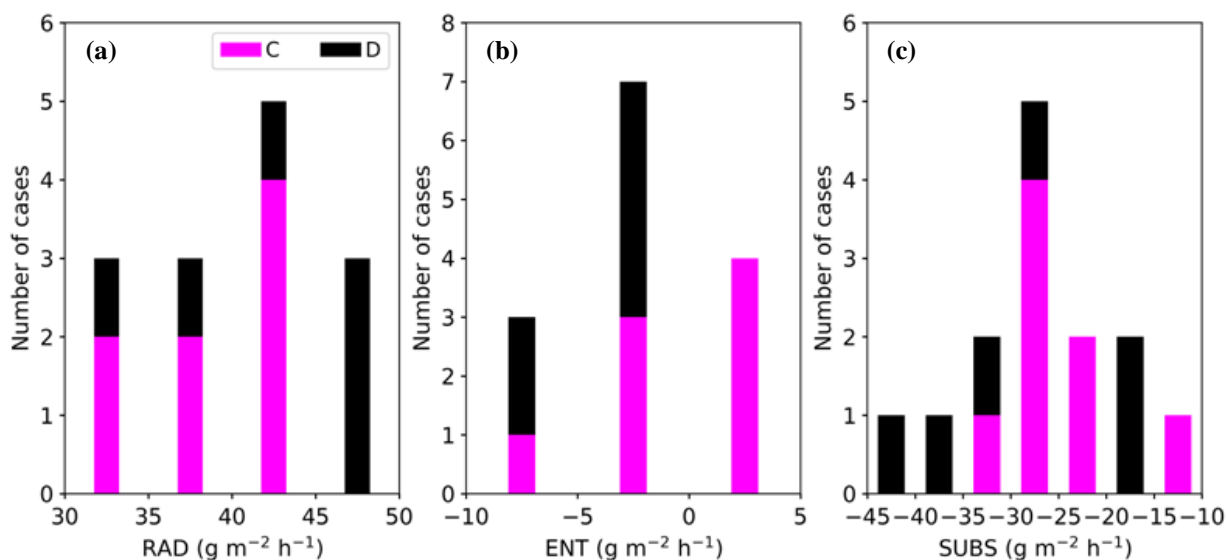
Figure 9 : Distributions of LWP budget terms RAD (a), ENT (b) and SUBS (c), derived from the 14 standard morning radiosoundings (Table A-1).

Figure 9 presents the distributions of RAD (Fig. 9a, Eq. 1.d), ENT (Fig. 9b, Eq. 1.b) and SUBS (Fig. 9c, Eq. 1.e) derived from the 14 radiosoundings considered in Figure 8 by the methodology described in section 3.1. The RAD term ranges within 30-50 g m^{-2} h^{-1}, with a median of 42 g m^{-2} h^{-1}. ENT varies between -10 and 5 g m^{-2} h^{-1}, indicating a smaller contribution to the LWP budget compared to RAD. The negative value of about -10 is consistent with the study of Pedruzo-Bagazgoitia et al. (2020), with a predominant role of temperature and humidity jumps at the cloud top, and a drying and warming effect of the entrainment. Among the 14 cases, several have a smaller contribution of ENT than this, some of them having even positive value for ENT, which means that the LLSC depth has more impact than the temperature and humidity jumps, so that the entrainment in those cases favours the deepening of the cloud. The term SUBS ranges between -45 and -10 g m^{-2} h^{-1}, with a median of around -27 g m^{-2} h^{-1}. It corresponds to as much as -0.4 to -0.9 times the RAD term, that is very significant. This is also consistent with Pedruzo-Bagazgoitia et al. (2020), (SUBS/RAD) approximately equal to -0.4 before sunrise. The answers to the two questions raised at the start of this section are:

1) We found similar results compared to Pedruzo-Bagazgoitia et al. (2020). However, the West African inland LLSC layer which develops within the monsoon flow is characterized by weaker temperature and humidity jumps, and smaller radiative cooling at its top as compared to marine stratiform clouds.

2) The three terms RAD, ENT and SUBS do not exhibit significant differences between the cases C and D (Fig. 9), because of similar cloud depth and thermodynamic characteristics. The slight differences in CBH and moisture jump across the cloud top between the two types of cases do not impact the LWP budget analysis.

By a series of sensitivity tests based on horizontal wind speed profiles, Pedruzo-Bagazgoitia et al. (2020) found that a wind shear at the cloud top before the sunrise, as such observed for the LLSC during DACCIWA (Lohou et al., 2020), accelerates the cloud deck breakup by generating dynamical turbulence which enhances the term ENT. However, they did not investigate the effect of wind shear underneath the LLSC.

From the 14 morning soundings considered in Fig. 8, we quantified the contribution of vertical shear to the production of turbulence at the LLSC top (Table A-1). We find it to be generally smaller than 20.10^{-5} s^{-2}, that is considerably smaller than the one imposed at the initialization of the LES experiments performed by Pedruzo-Bagazgoitia et al. (2020). However, this contribution in the subcloud layer is mostly higher than 50.10^{-5} s^{-2} (Figure 4c). Thus, the dynamical instability induced by the NLLJ is more important below the LLSC than above. This should imply that the mechanical turbulence driven by the NLLJ impacts much more the turbulent fluxes below the LLSC base than the entrainment of ambient air from above.

5 Evolution of the LLSC layer under daytime conditions

In this section, the evolution of the LLSC during the convective phase until its breakup is analyzed.

5.1 The three scenarios of evolution

The evolution of LLSC during the convective phase is first analyzed according to the ceilometer-derived CBHs temporal change relatively to the surface-based LCLs. From this point of view, all the cases C evolve quite similarly during the convective phase, while two distinct scenarios are observed among the cases D (hereafter named DC for "decoupled-coupled" and DD for "decoupled-decoupled"). Each of the three scenarios is illustrated by one typical example; the LLSC occurrence on 07-08 July (Fig. 10a) for scenario C, 25-26 June (Fig. 10b) and 04-05 July (Fig. 10c) for scenarios DC and DD respectively.
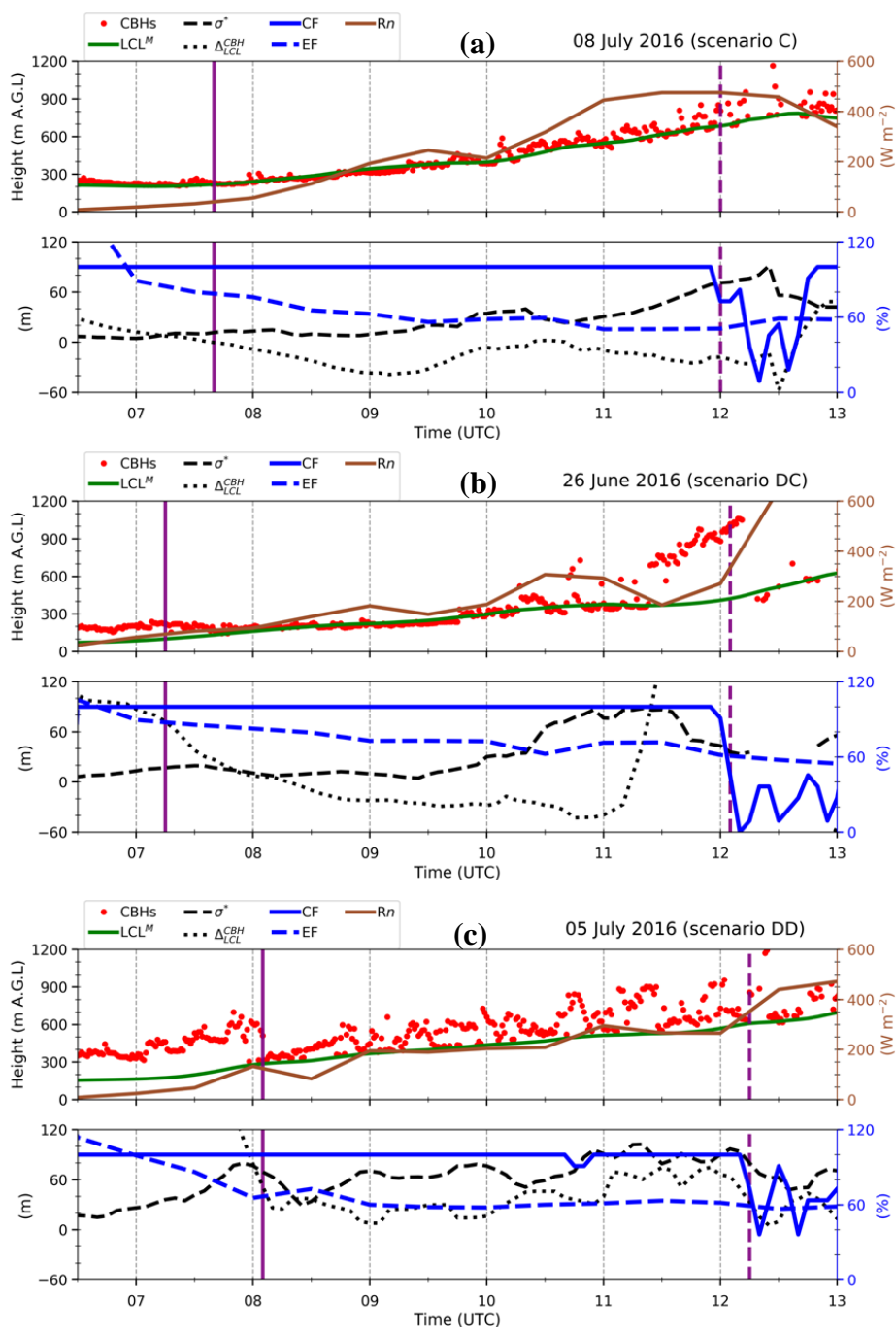
Figure 10 : Illustration of the three scenarios of LLSC evolution during the convective phase: **(a)** 8 July for scenario C, **(b)** 26 June for scenario DC and **(c)** 5 July for scenario DD. The top panels present the ceilometer-derived CBHs, the lifting condensation level (LCL) and the net radiation (Rn) measured at surface. The bottom panels gather the cloud fraction (CF), the evaporative fraction (EF in %), the standard deviation of the cloud base height (σ^*) and the distance between the cloud base and the LCL (Δ_{LCL}^{CBH}). The vertical solid and dashed lines indicate T_i and T_b, respectively.

Whether the CBHs is close to the LCL (Fig. 10a) or not (Fig. 10b and c), it has a low variability before 07:00 UTC in these three illustrative cases, indicating a quite horizontally homogenous base of the LLSC layer before the start of the convective phase (as already seen in the previous section). The CBHs and the LCL in scenario C lift together after 07:30 UTC, due to thermal convective conditions in the subcloud layer. After 09:00 UTC, σ* increases gradually, but the lower
5 bases always fit with the LCL, with Δ_{LCL}^{CBH} ranging between 0 and -40 m (Fig. 10a, lower panel). This can be interpreted as a progressive change in the LLSC base structure which is more and more heterogeneous in height but the cloud layer remains coupled with the surface all along. The evolution from stratus to stratocumulus and eventually to cumulus can hardly be established with the use of CBHs only, but CBHs already show a clear evolution of the homogeneous low stratus towards a more heterogeneous low cloud structure until the LLSC breakup time, established when CF decreases to less than 90%,
10 which happens at 12:00 UTC on the 08 July.

The LLSC in the scenario DC (Fig. 10b) is decoupled from the surface at the end of the stratus phase. The LCL starts to rise at 07:00 UTC and joins the LLSC base about 1 hour later, indicated by a decrease of the Δ_{LCL}^{CBH} down to zero (Fig. 10b, lower panel). After the coupling, the scenario DC is very similar to the scenario C and will be further commented in the last section.

15 The evolution of the LLSC in the scenario DD (Fig. 10c) is quite different compared to the two others. The LLSC layer remains decoupled from the surface until 08:00 UTC as shown by the significant departure between LCL and CBHs ($\Delta_{LCL}^{CBH} > 120\ m$, Fig. 10c, lower panel) due to a similar lifting rate of both levels. After 08:00 UTC, a new cloud layer with a base very close to the LCL ($\Delta_{LCL}^{CBH} < 40\ m$), is detected 200 m below the LLSC. The values of σ* much larger than 60 m after 08:30 UTC indicate that, this new cloud layer rapidly turns to shallow cumulus clouds. Unfortunately, the ceilometer is not
20 able to monitor both cloud layers separately. But one can suppose that the LLSC formed during the night remained above the cumulus clouds layer after sunrise. The higher CBHs detected by the ceilometer after 09:00 UTC are the overlying stratus layer base (about 200 m higher). The cumulus and stratus layers can clearly be seen on the visible and infra-red full sky cameras (not shown).

Among the 13 cases D observed at the end of the stratus phase, 8 follow the scenario DD and 5 follow the scenario DC
25 during the convective phase (Table A-1). The main difference between the three scenarios is that the first shallow convective clouds form when the LLSC breaks up in scenarios C and DC, whereas in the scenario DD, shallow cumulus clouds form below the LLSC layer before it breaks up. Similar transitions were reported by previous observational and modelling studies on the stratiform low clouds (Ghonima et al., 2016; Pedruzo-Bagazgoitia et al., 2020; Price, 1999; Xiao et al., 2011). Especially, the transition of scenario DD is part of the conceptual model for marine stratocumulus (Wood, 2012; Xiao et al.,
30 2011). In such conditions, the underlying cumulus clouds act to intermittently and locally couple the stratocumulus layer with the surface (Wood, 2012).

One can wonder what conditions lead the LLSC to either be coupled to the surface in the scenario DC, or remain decoupled with the formation of an underlying cumulus layer in the scenario DD. No relevant differences in macrophysical

characteristics of LLSC (base and depth) were found between the two scenarios at the end of the stratus phase and beginning of the convective phase (not shown). One could argue that the low number of cases does not allow a robust statistic, but the LLSCs with low bases are not systematically those which will be coupled to the surface at the beginning of the convective phase. Eventually, the four parameters presented in Fig. 8, and summarizing the thermodynamical conditions in the subcloud

5   layer and above the LLSC, are not fundamentally different either between DC and DD scenarios. The relative humidity in the subcloud layer at the beginning of the stratus phase is larger than 95 % whatever the case, and the difference between the different scenarios is smaller than 2 % which is about the accuracy of the measurement or lower. Consequently, alternative approaches are needed to identify the processes involved in the coupling of LLSC during the convective phase.

   In conclusion, the nature of coupling between the LLSC and the surface during the convective phase appears to be the key
10   factor determining the way by which the transition towards shallow convective clouds takes place. When the LLSC is coupled to the surface (cases C and DC), it is the breakup of the cloud deck which leads to the formation of different low-level clouds type (stratocumulus or cumulus). When the LLSC is decoupled from the surface (cases D), the convective clouds firstly form below it. In the next paragraphs, we deeply analyze the different scenarios of the LLSC evolution.
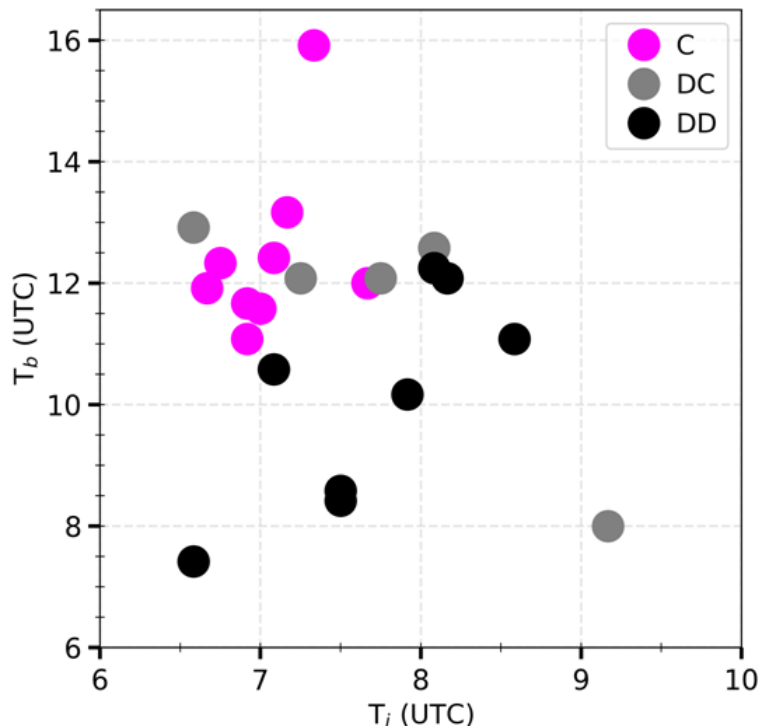
Figure 11 : LLSC breakup time (T_b) against the time at which the low cloud coverage is impacted by thermally-driven turbulence (T_i) for the 22 selected cases (Table A-1). Colors stand for the three scenarios.

5.2 Surface-convection and breakup times

The time T_i indicates when the low cloud coverage is influenced by the surface-buoyancy-driven turbulence and T_b when the low cloud breaks up. T_i is defined differently according to the scenario. For the scenario C, T_i corresponds to the time when the LLSC base starts to lift together with the LCL. After sensitivity tests, T_i is defined as the first time when LCL^M increases to at least 5 m above its value at 06:30 UTC. For the scenario DC, T_i corresponds to the time when the rising LCL reaches the LLSC base, that is when the LLSC is coupled to the surface ($\Delta_{LCL}^{CBH} < 75$ m, which is also the threshold used to sort out C and D cases at the end of the stratus phase in section 4.1). For the scenario DD, T_i is the first time when new low clouds appear below the LLSC deck. As these clouds are coupled to the surface T_i is also determined when Δ_{LCL}^{CBH} decreases to less than 75 m.

Figure 11 displays T_b and T_i for the 22 LLSC cases (Table A-1). T_i ranges between 06:30 and 09:15 UTC. T_b varies between 07:30 and 16:00 UTC, with breakup times occurring before 12:00 UTC for 72% of the cases. The latter result is consistent with the findings of Dione et al. (2019) who used the infrared images from the cloud camera to define the LLSC lifetime. One can see that the LLSC breakup time is not linked to the time at which it starts to rise or at which the underlying clouds form.

For the scenario C, T_i hardly changes from one case to the other. It ranges between 06:40 and 08:00 UTC, that is not long after the sunrise (06:30 UTC). The LLSC persists at least 4.5 hours and breaks up between 11:00 and 16:00 UTC. The latest breakup time occurring at 16:00 UTC corresponds to the 02-03 July case for which the hydrometeors radar reflectivity from the cloud radar reveals light precipitations above the LLSC layer during the first hours of the convective phase (not shown) while nothing was recorded by the surface rain gauge. This external forcing, able to enhance the liquid water content in the LLSC layer, is certainly responsible for this late breakup. Because this case is an exception and cannot easily be compared to the others, it is not considered here after.

For 4 DC cases out of 5, T_i and T_b are very close to the values observed for C cases. This means that the stable stratification in the subcloud layer before the convective phase (which allowed the classification of this case as decoupled during the stratus phase) is rapidly eroded after sunrise and does not seem to impact the breakup time. The case for which T_b occurred at 08:00 UTC (16-17 July) is removed in the following as well, because the LLSC breaks up before the LCL reaches its base.

The scenario DD presents the largest variation ranges of T_i (between 06:35 UTC and 09:00 UTC) and T_b (between 07:00 UTC and 13:00 UTC). The most striking result is that the LLSC in scenario DD often breaks up earlier than in scenarios C and DC.

Following the LES of Pedruzo-Bagazgoitia et al. (2020), the start of the convective phase leads to three main changes in LWP equation. First, the radiative cooling (RAD term) decreases due to the solar heating at the cloud top. Second, the ENT term also strongly decreases because the thermally-driven convection enhances the entrainment of dry and warm air from

aloft in the LLSC. Third, the BASE term, which was close to zero during the stratus phase, comes into play during the convective phase and contributes positively to $\frac{\partial LWP}{\partial t}$. Despite the BASE term, the strong decrease of both ENT and RAD makes $\frac{\partial LWP}{\partial t}$ negative one hour after the sunrise. The RAD and ENT terms cannot be estimated during the convective phase with the dataset acquired at Savè because several data are missing, and, among them, the CTH.

5   The scenarios C and DC during the convective phase are very close to the case simulated in Pedruzo-Bagazgoitia et al. (2020) and one can expect a quite similar evolution of the terms involved in the LWP prognostic equation. Conversely, the scenario DD might be very different. The LLSC breaks up earlier, mostly before or around 10:30 UTC, when it is decoupled from the surface layer, likely due to a weaker BASE term. This hypothesis is supported by the findings of van der Dussen et al. (2014) who found that stratiform cloud coupled to the surface moisture are more resistant to cloud-thinning related

10   processes such as the entrainment of dry and warm air into the cloudy layer. The stronger variability of the breakup time for DD cases may come from the fact that the LLSC thinning depends on its interaction with the underlying cloud layer. If the latter penetrates the LLSC, local coupling can happen which induces a homogeneous layer from surface to the cloud top, but, at the same time, the entrainment at the cloud top is enhanced by the cumulus vertical development (Wang and Lenschow, 1995).

15   The LLSC breakup time impacts the radiative budget at surface over the day, then the surface fluxes, and consequently, the vertical development of the ABL (Lohou et al., 2020). The later develops up to 900 m when the LLSC breaks up at 09:00 UTC and is 30% lower when the LLSC breaks up at 12:00 UTC.

5.3 Evolution of the LLSC horizontal structure for C and DC cases

20   The changes in the LLSC horizontal structure for C and DC scenarios is now further analyzed based on the evolution of the LLSC base and its standard deviation σ^*. The cases DD are excluded from this analysis because the macrophysical characteristics of the associated LLSC cannot be determined after the underlying cloud formation. As illustrated in Fig. 10a and b, the elevation rate of the LCL, and consequently of the LLSC base, may change a lot from one case to the other. It is about 108 m h^{-1} and 67 m h^{-1} for 8 July and 26 June, respectively. One could expect that the higher this rate, the higher R_n,

25   and the more intense is the thermally-driven convection in the subcloud layer as well as the corresponding BASE term. However, no clear link is pointed out between T_b and this elevation rate of the LLSC base (not shown).
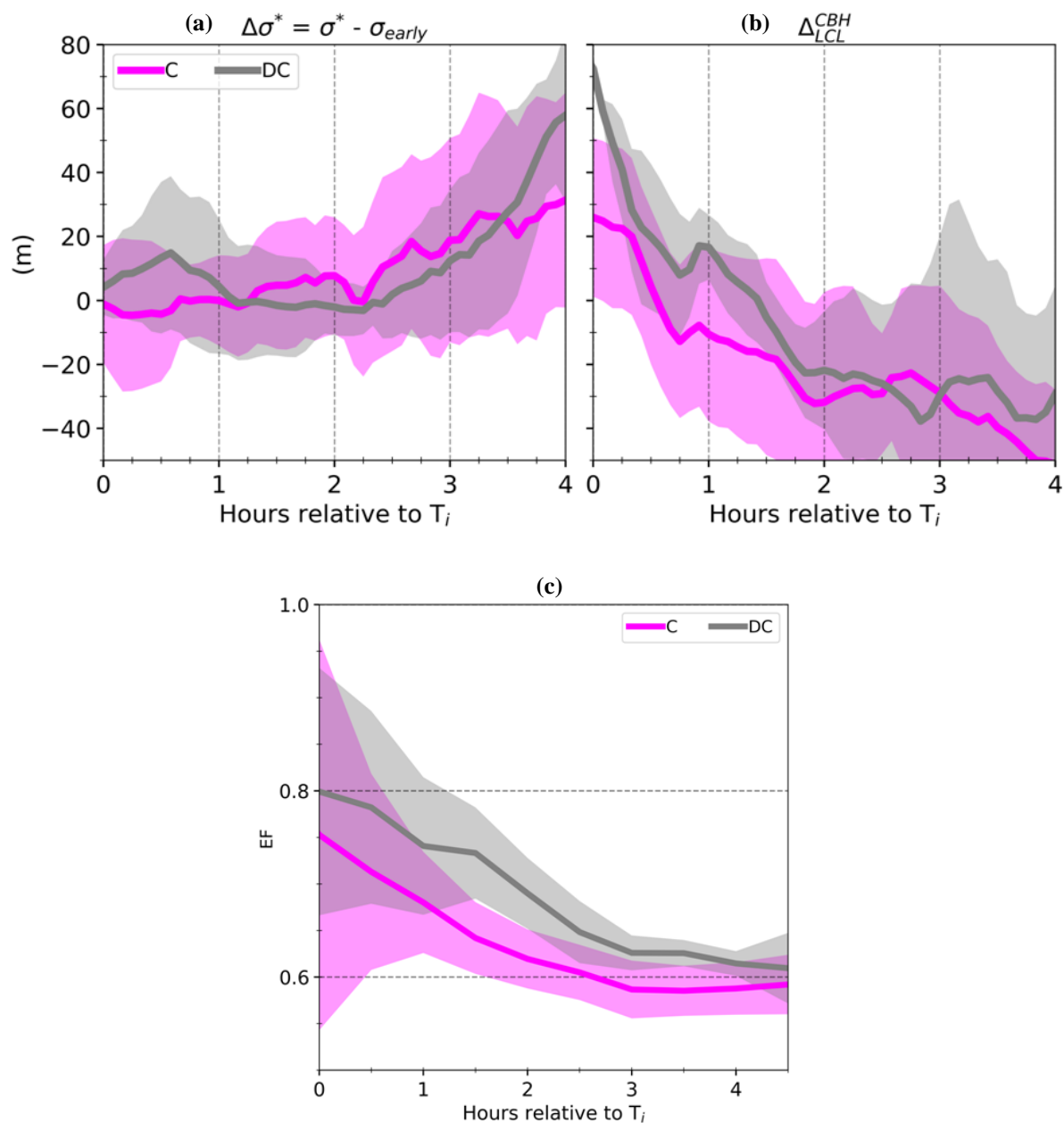
Figure 12 : Evolution of, **(a)** Δσ*, which is the difference between σ* and its median over the period from 04:00 to 06:30 UTC (σ$_{Early}$), and, **(b)** Δ_{LCL}^{CBH}, **(c)** the evaporative fraction (EF) at surface, for C (coupled) and DC (decoupled-coupled) scenarios. The solid lines indicate the median and shaded areas represent the standard deviation. The time is expressed in hours relative to T$_i$.

Contrary to the LLSC base height, σ^* has a common tendency among all the C and DC cases. The evolution of σ^* with time compared to its value at T_i, σ_{Early}, is presented in Fig. 12a. A four hour-period is considered here because it is the smallest duration between T_i and T_b (Fig. 11) for the 12 C and DC cases included in this statistic. As also illustrated in Fig.

5   10a and Fig. 10b, σ^* remains close to σ_{Early} during at least two hours after T_i (until 09:00 UTC for 8 July and 09:30 UTC for 26 July). Consequently, during this period, the structure of the LLSC bases remains quasi-unchanged in time. Afterwards, σ^* progressively increases during at least 2 hours until the breakup. From T_i to the breakup, Δ_{LCL}^{CBH} remains lower than 70 m, with even a slight decrease in the first two hours (Fig. 12b), suggesting an enhancement of the coupling due to an increase thermally-driven turbulence in the subcloud layer. The combination of very heterogeneous LLSC base and the lowest ones

10   close to the LCL during the few hours before T_b, indicates that some of the bases are coupled to the surface but some tend to be decoupled from the surface.

Eventually, the evolution of σ^* and Δ_{LCL}^{CBH} (Fig. 12) allows to define two periods between T_i and T_b: (1) the two first hours after T_i during which the LLSC is fully coupled to the surface and the homogeneity of its base is not affected yet, and, (2) the few hours before T_b during which the base of the LLSC layer becomes more and more heterogeneous and intermittently

15   decoupled from the surface. This latter tendency can be seen in Fig. 10a upper panel after 11:00 UTC and in Fig. 10b lower panel after 10:15 UTC. A decoupling of the stratiform cloud from the surface is also observed about half an hour before the cloud deck breakup in Pedruzo-Bagazgoitia et al. (2020) simulations.

The bottom panels of Fig. 10 present the evolution of the evaporative fraction (EF) at the surface for the illustrative cases. The Figure 12c displays the medians of this parameter over all C and DC cases. Defined as the ratio of LHF to (LHF + SHF),

20   EF larger than 0.5 means that the evapo-transpiration dominates over the warming. This is in average the case in Savè during the DACCIWA campaign (Kalthoff et al., 2018). Figure 12c shows that the median of EF decreases from around 0.75 at T_i to 0.6 at the LLSC breakup. The predominance of the evapo-transpiration over the sensible heat flux, particularly during the two first hours after T_i, and the full coupling of the LLSC to the surface, might contribute to maintain the LLSC through the BASE term. The LLSC base is indeed strongly homogeneous. The decrease of EF and its stabilisation at 0.6 implies a faster

25   increase of SHF than LHF at surface. One can then expect a larger contribution of $\overline{w'\theta_l'}^b$ and a smaller from $\overline{w'q_t'}^b$ in BASE term with time. This could favour the convection in the cloud which enhances the entrainment, at the expense of the cloud moistening by the underlying turbulent mixing. In addition to this, the final intermittent decoupling of the LLSC from the surface likely contribute, together with the decrease of RAD and ENT (Pedruzo-Bagazgoitia et al., 2020), to the LLSC breakup.

30   It appears that, the LLSC and the timing of its evolution in the scenarios C and DC are very similar during the convective phase. In these scenarios, the LLSC keeps the same characteristics in terms of base height and homogeneity during two hours after T_i. Afterwards and until its breakup, the LLSC becomes more and more heterogeneous and intermittently

decoupled from the surface. These two steps are in phase with the evolution of the EF which likely impacts the BASE term which is the only positive contribution in the LWP equation.
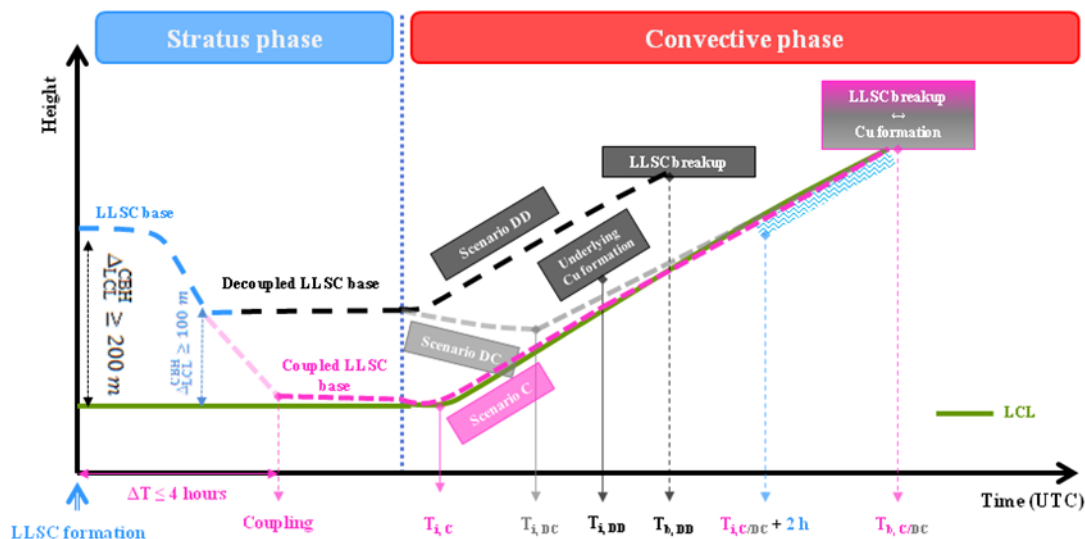
Figure 13 : Schematic representation of the main findings of this study. It portrays the typical LLSC evolutions over the southern West Africa during the Monsoon season. The different scenarios and their characteristic times are illustrated. Their typical values are given in the table at the bottom. The different lines represent the evolution of the LLSC base (dashed line) and the surface-based LCL (solid green line). The shaded blue pattern marks the characteristic time interval for the scenario C and DC in which the LLSC base becomes more and more heterogeneous until the cloud deck breakup.

6 Summary and conclusion

The breakup of the almost daily LLSC during Monsoon season in southern West Africa is the object of this study. It is
5 based on the analysis of a set of twenty-two precipitation-free LLSC occurrences observed during the DACCIWA field experiment at Savè supersite. The diurnal cycle of the LLSC consists of 4 main stages and this study addresses the two latest,

the *stratus* and *convective* phases. We used the ground-based observational data collected by ceilometer and cloud radar for macrophysical properties of the cloud layer, energy balance and weather stations for the atmospheric conditions near the surface, and, radiosoundings and UHF wind profiler for the thermodynamical and dynamical conditions within the low-troposphere. From these measurements, some diagnostics of the LLSC layer are estimated, including: the cloud-base height,

5   the cloud coverage fraction, the cloud base homogeneity and the cloud coupling with the surface. The latter aspect was assessed by the distance between the LLSC base and the lifting condensation level; the cloud layer is coupled to the surface when these two levels coincide. Our main results are summarized in Fig. 13 by a schematic illustration.

At the beginning of the stratus phase (after 22:00 UTC), the LLSC is decoupled from the surface in all the studied cases, expect in one (dashed blue lines in Fig. 13). Within the following four hours, in 9 among the 22 cases, the LLSC base lowers

10   in such way that the cloud layer gets coupled to the surface (referenced as cases C with magenta dashed line in Fig. 13). In the 13 other cases (referenced as cases D with dark dashed line in Fig. 13), the LLSC remains decoupled from the surface. The weak thermodynamical differences observed between C and D cases at Savè can hardly explain the coupling which occurs in C cases. However, the cases C occurred preferentially between 27 June and 8 July 2016, a period with a well-established Monsoon flow over West-Africa, especially over DACCIWA investigated area. Most of the cases D are observed

15   during the Monsoon onset period or during disturbed sub-periods after the 08 July 2016. If the synoptic conditions of the Monsoon flow play a role on the coupling of stratus to the surface, it could be through the thermodynamical conditions, which were not highlighted with Savè data set. It could also be through large scale dynamical parameters like large scale subsidence, which is an important factor in LWP budget and could not be determined precisely for every day with Savè data set. The analyses of the stable and jet phase by Adler et al. (2019) and Babić et al. (2019a,b) outline a complex imbrications

20   of different processes in LLSC formation. Similarly, we conclude that the coupling of the LLSC to the surface during the stratus phase is also based on different processes for which a slight intensity change may have an important impact.

The Savè data set allowed us to estimate some of the terms of the LWP budget at the end of the stratus phase. The radiative cooling and the entrainment terms, which are among the most important terms at that time of the LLSC cycle are very close to those found by Pedruzo-Bagazgoitia et al. (2020) in the numerical study of a DACCIWA case. Since the LLSC

25   layer develops in the Monsoon flow, the LWP budget terms are quite different from those described in previous studies, and especially those characterizing marine stratocumulus. This is due to drastically weaker inversion jumps in temperature and humidity at cloud top during DACCIWA field campaign which impacts the radiative cooling and the entrainment terms.

During the convective phase of the LLSC diurnal cycle, a new separation occurs among the D cases. In some of them, the LLSC couples to the surface while the lifting condensation level rises with the thermally-driven convection at the surface.

30   Therefore, the LLSC deck may follow three scenarios until its breakup: (1) the scenario C (followed by all the C cases of the stratus phase), (2) the scenario DC for "decoupled-coupled" (followed by some of D cases in dashed grey lines in Fig. 13), and, (3) the scenario DD for "decoupled-decoupled" (followed by the other D cases). The scenarios C and DD are the most frequent among the 22 studied cases with 9 and 8 occurrences respectively. The reason why the cases D follow DC or DD was not clearly identified.

Typically, the scenarios C and DC are quite similar and consist of two steps: (ii) the first two hours during which the LLSC layer lifts but remains fully coupled to the surface and the homogeneity of its base is not affected yet, (ii) the few hours preceding the breakup time during which the cloud layer is sometime decoupled from the surface as its base becomes more and more heterogeneous. In these two scenarios, the breakup of the LLSC deck leads to a transition towards shallow

5 cumulus clouds. That occurs at around 11:00 UTC or later, approximately more than 4.5 hours after the LLSC starts to lift. In the scenario DD, cumulus clouds, triggered by convectively mixed layer, form below the LLSC deck before its breakup. The breakup time in this scenario varies strongly between 07:30 UTC and noon. But in most of the cases, it occurs before 11:00 UTC. The earlier breakup occurring in the scenario DD outlines the importance of the coupling with surface for the LLSC maintenance after the sunrise. Thus, we conclude that, in SWA conditions, the coupling between the LLSC and the

10 surface is a key factor for its evolution during daylight hours. It determines the LLSC lifetime and the way by which the transition towards shallow cumulus occurs. The coupled LLSC last longer and can therefore more significantly impact the surface energy budget over the day.

These results can help to identify the weaknesses in global climate and weather model simulations for a better representation of WAM features. The influence of middle-level clouds on the LLSC remains also an opened question. It is

15 not objectively addressed in this study.

Data availability. The data used in this study are available in the BAOBAB (Base Afrique de l'Ouest Beyond AMMA Base) database (https://baobab.sedoo.fr/DACCIWA/) (Derrien et al., 2016; Handwerker et al., 2016; Kohler et al., 2016; Wieser et

20 al., 2016).

Author contributions. FL, NK, ML, BA and XPB performed the measurements at Savè supersite. MZ processed the data and carried out the analysis with contributions from FL and ML. MZ wrote the paper with contributions from all co-authors.

25 *Competing interests*. The authors declare that they have no conflict of interest.

Appendix A : Overview of the LLSC characteristic

Synoptic conditions	Onset		Post-Onset																		Recovery		
Months	June 2016											July 2016											
Day-D+1	20	22	26	27	29	30	01	02	03	04	05	06	07	08	10	11	17	18	19	27	28	29
IOP N°	–	–	03	04	–	–	05	06	06	–	07	–	–	08	–	09	–	11	–	14	–	–
CBH	206	370	204	226	249	174	53	70	91	100	277	147	292	253	299	380	306	338	136	260	206	208
Depth	813	499	185	404	381	306	607	320	–	470	502	452	337	407	380	–	384	412	313	385	573	–
Shear+	6.1	2.1	0.8	7.0	1.0	0.7	0.6	5.0	–	36.9	5.3	11.2	16.7	9.6	–	–	–	–	3.0	–	–	–
$\theta^- - 290$	7.2	7.5	6.6	7.5	7.4	7.2	6.9	6.6	–	6.4	7.7	7.2	8.2	7.8	–	–	–	–	6.3	–	–	–
$\Delta\theta_l$	3.6	2.5	1.5	2.2	2.2	1.6	3.5	1.9	–	4.4	4.1	2.6	1.8	2.6	–	–	–	–	2.4	–	–	–
q^-	16.7	15.7	16.0	16.8	16.4	16.9	17.0	16.8	–	16.8	16.3	17.0	16.7	16.9	–	–	–	–	16.2	–	–	–
Δq_t	-3.0	-2.0	-0.2	-1.4	-1.2	-1.4	-1.1	-0.6	–	-0.2	-1.5	-1.0	-1.2	-0.8	–	–	–	–	-0.1	–	–	–
RAD	46.1	47.9	39.6	39.3	43.3	43.1	32.6	42.4	–	32.1	33.1	37.4	45.9	41.7	–	–	–	–	42.7	–	–	–
ENT	-1.0	-5.8	-1.6	-2.9	-3.3	-6.8	1.6	2.2	–	-2.9	-6.2	0.6	-3.4	-0.8	–	–	–	–	0.3	–	–	–
SUBS	-41.4	-38.0	-20.8	-28.6	-29.7	-32.7	-22.4	-29.9	–	-13.6	-16.1	-25.8	-34.2	-25.9	–	–	–	–	-22.1	–	–	–
T_i	0835	0730	0715	0700	0810	0705	0710	0655	0720	0655	0805	0640	0635	0740	0705	0755	0910	0730	0645	0745	0635	0805
T_b	1105	0835	1205	1135	1205	1225	1310	1140	1555	1105	1215	1155	1255	1200	1035	1010	0800	0825	1220	1205	0725	1235

LLSC at the end of the stratus phase (section 4); LLSC during Convective phase (section 5)

Table A-1 : Summary of the LLSC characteristic at the end of the stratus phase (section 4) and during the convective phase (section 5) for the 22 occurrences at Savè supersite analyzed in this study. The Day-D+1 of the night-to-day transition and the eventual corresponding IOP number are indicated. The main synoptic conditions defined by Knippertz et al. (2017) in which they fall are mentioned at the top. The Cloud base height (CBH in m a.g.l) and depth (m) are estimated by the ceilometer and cloud radar measurements. The wind shear at the cloud top (Shear+), the thermodynamical properties of the cloud, θ^- and $\Delta\theta_l$ in K, q^-, Δq_t and g kg^{-1} as well as the terms RAD, ENT and SUBS (in g m^{-2} h^{-1}) are derived from 05:00 UTC standard radiosoundings. They are only estimated for the 14 cases for which the radiosonde flew into the LLSC layer. The characteristic times of the evolution during the convective phase, the surface-convection influence (T_i) and breakup (T_b) times are in UTC in the format HHMM. The background colour stands for the LLSC behaviour. The cases C (coupled LLSC) and D (decoupled LLSC) at the end of the stratus phase are in magenta and black respectively. The cases D in which the LLSC describes DC (DD), for decoupled-coupled (decoupled-decoupled) during the convective phase are in grey (black).

References

Adler, B., Kalthoff, N. and Gantner, L.: Nocturnal low-level clouds over southern West Africa analysed using high-resolution simulations, Atmospheric Chemistry and Physics, 17(2), 899–910, doi:10.5194/acp-17-899-2017, 2017.

5 Adler, B., Babić, K., Kalthoff, N., Lohou, F., Lothon, M., Dione, C., Pedruzo-Bagazgoitia, X. and Andersen, H.: Nocturnal low-level clouds in the atmospheric boundary layer over southern West Africa: an observation-based analysis of conditions and processes, Atmospheric Chemistry and Physics, 19(1), 663–681, doi:10.5194/acp-19-663-2019, 2019.

Babić, K., Adler, B., Kalthoff, N., Andersen, H., Dione, C., Lohou, F., Lothon, M. and Pedruzo-Bagazgoitia, X.: The observed diurnal cycle of low-level stratus clouds over southern West Africa: a case study, Atmospheric Chemistry and
10 Physics, 19(2), 1281–1299, doi:10.5194/acp-19-1281-2019, 2019a.

Babić, K., Kalthoff, N., Adler, B., Quinting, J. F., Lohou, F., Dione, C. and Lothon, M.: What controls the formation of nocturnal low-level stratus clouds over southern West Africa during the monsoon season?, Atmos. Chem. Phys., 19(21), 13489–13506, doi:10.5194/acp-19-13489-2019, 2019b.

Bretherton, C. S., Krueger, S. K., Wyant, M. C., Bechtold, P., Van Meijgaard, E., Stevens, B. and Teixeira, J.: A GCSS
15 Boundary-Layer Cloud Model Intercomparison Study Of The First Astex Lagrangian Experiment, Boundary-Layer Meteorology, 93(3), 341–380, doi:10.1023/A:1002005429969, 1999.

Copernicus Climate Change Service: ERA5-Land hourly data from 2001 to present, , doi:10.24381/CDS.E2161BAC, 2019.

Dearden, C., Hill, A., Coe, H. and Choularton, T.: The role of droplet sedimentation in the evolution of low-level clouds over southern West Africa, Atmos. Chem. Phys., 18(19), 14253–14269, doi:10.5194/acp-18-14253-2018, 2018.

20 Deetz, K., Vogel, H., Knippertz, P., Adler, B., Taylor, J., Coe, H., Bower, K., Haslett, S., Flynn, M., Dorsey, J., Crawford, I., Kottmeier, C. and Vogel, B.: Cloud and aerosol radiative effects as key players for anthropogenicchanges in atmospheric dynamics over southernWest Africa, Atmos. Chem. Phys. Discuss., 1–36, doi:10.5194/acp-2018-186, 2018.

Dione, C., Lohou, F., Lothon, M., Adler, B., Babić, K., Kalthoff, N., Pedruzo-Bagazgoitia, X., Bezombes, Y. and Gabella, O.: Low-level stratiform clouds and dynamical features observed within the southern West African monsoon, Atmos. Chem.
25 Phys., 19(13), 8979–8997, doi:10.5194/acp-19-8979-2019, 2019.

van der Dussen, J. J., de Roode, S. R. and Siebesma, A. P.: Factors Controlling Rapid Stratocumulus Cloud Thinning, J. Atmos. Sci., 71(2), 655–664, doi:10.1175/JAS-D-13-0114.1, 2014.

van der Dussen, J. J., de Roode, S. R. and Siebesma, A. P.: How large-scale subsidence affects stratocumulus transitions, Atmos. Chem. Phys., 16(2), 691–701, doi:10.5194/acp-16-691-2016, 2016.

30 Duynkerke, P. G., de Roode, S. R., van Zanten, M. C., Calvo, J., Cuxart, J., Cheinet, S., Chlond, A., Grenier, H., Jonker, P. J., Köhler, M., Lenderink, G., Lewellen, D., Lappen, C.-L., Lock, A. P., Moeng, C.-H., Müller, F., Olmeda, D., Piriou, J.-M., Sánchez, E. and Sednev, I.: Observations and numerical simulations of the diurnal cycle of the EUROCS stratocumulus case, Q. J. R. Meteorol. Soc., 130(604), 3269–3296, doi:10.1256/qj.03.139, 2004.

Faloona, I., Lenschow, D. H., Campos, T., Stevens, B., van Zanten, M., Blomquist, B., Thornton, D., Bandy, A. and Gerber,
35 H.: Observations of Entrainment in Eastern Pacific Marine Stratocumulus Using Three Conserved Scalars, J. Atmos. Sci., 62(9), 3268–3285, doi:10.1175/JAS3541.1, 2005.

Flamant, C., Knippertz, P., Fink, A. H., Akpo, A., Brooks, B., Chiu, C. J., Coe, H., Danuor, S., Evans, M., Jegede, O., Kalthoff, N., Konaré, A., Liousse, C., Lohou, F., Mari, C., Schlager, H., Schwarzenboeck, A., Adler, B., Amekudzi, L., Aryee, J., Ayoola, M., Batenburg, A. M., Bessardon, G., Borrmann, S., Brito, J., Bower, K., Burnet, F., Catoire, V., Colomb, A., Denjean, C., Fosu-Amankwah, K., Hill, P. G., Lee, J., Lothon, M., Maranan, M., Marsham, J., Meynadier, R., Ngamini, J.-B., Rosenberg, P., Sauer, D., Smith, V., Stratmann, G., Taylor, J. W., Voigt, C. and Yoboué, V.: The Dynamics-Aerosol-Chemistry-Cloud Interactions in West Africa field campaign: Overview and research highlights, Bull. Amer. Meteor. Soc., doi:10.1175/BAMS-D-16-0256.1, 2017.

Garratt, J. R.: The Atmospheric Boundary Layer, Cambridge University Press., 1994.

Ghonima, M. S., Heus, T., Norris, J. R. and Kleissl, J.: Factors Controlling Stratocumulus Cloud Lifetime over Coastal Land, J. Atmos. Sci., 73(8), 2961–2983, doi:10.1175/JAS-D-15-0228.1, 2016.

Handwerker, J., Scheer, S. and Gamer, T.: DACCIWA field campaign, Savè super-site, Cloud and precipitation, , doi:10.6096/dacciwa.1686, 2016.

Hannak, L., Knippertz, P., Fink, A. H., Kniffka, A. and Pante, G.: Why Do Global Climate Models Struggle to Represent Low-Level Clouds in the West African Summer Monsoon?, J. Climate, 30(5), 1665–1687, doi:10.1175/JCLI-D-16-0451.1, 2017.

Kalthoff, N., Lohou, F., Brooks, B., Jegede, G., Adler, B., Babić, K., Dione, C., Ajao, A., Amekudzi, L. K., Aryee, J. N. A., Ayoola, M., Bessardon, G., Danuor, S. K., Handwerker, J., Kohler, M., Lothon, M., Pedruzo-Bagazgoitia, X., Smith, V., Sunmonu, L., Wieser, A., Fink, A. H. and Knippertz, P.: An overview of the diurnal cycle of the atmospheric boundary layer during the West African monsoon season: results from the 2016 observational campaign, Atmospheric Chemistry and Physics, 18(4), 2913–2928, doi:10.5194/acp-18-2913-2018, 2018.

Knippertz, P., Fink, A. H., Schuster, R., Trentmann, J., Schrage, J. M. and Yorke, C.: Ultra-low clouds over the southern West African monsoon region, Geophysical Research Letters, 38(21), doi:10.1029/2011GL049278, 2011.

Knippertz, P., Coe, H., Chiu, J. C., Evans, M. J., Fink, A. H., Kalthoff, N., Liousse, C., Mari, C., Allan, R. P., Brooks, B., Danour, S., Flamant, C., Jegede, O. O., Lohou, F. and Marsham, J. H.: The DACCIWA Project: Dynamics–Aerosol–Chemistry–Cloud Interactions in West Africa, Bulletin of the American Meteorological Society, 96(9), 1451–1460, doi:10.1175/BAMS-D-14-00108.1, 2015.

Knippertz, P., Fink, A. H., Deroubaix, A., Morris, E., Tocquer, F., Evans, M. J., Flamant, C., Gaetani, M., Lavaysse, C., Mari, C., Marsham, J. H., Meynadier, R., Affo-Dogo, A., Bahaga, T., Brosse, F., Deetz, K., Guebsi, R., Latifou, I., Maranan, M., Rosenberg, P. D. and Schlueter, A.: A meteorological and chemical overview of the DACCIWA field campaign in West Africa in June–July 2016, Atmospheric Chemistry and Physics, 17(17), 10893–10918, doi:10.5194/acp-17-10893-2017, 2017.

Kohler, M., Kalthoff, N., Seringer, J. and Kraut, S.: DACCIWA field campaign, Savè super-site, Surface measurements, , doi:10.6096/dacciwa.1690, 2016.

Lilly, D. K.: Models of cloud-topped mixed layers under a strong inversion, Q.J.R. Meteorol. Soc., 94(401), 292–309, doi:10.1002/qj.49709440106, 1968.

van der Linden, R., Fink, A. H. and Redl, R.: Satellite-based climatology of low-level continental clouds in southern West Africa during the summer monsoon season: Low-level clouds in southern West Africa, Journal of Geophysical Research: Atmospheres, 120(3), 1186–1201, doi:10.1002/2014JD022614, 2015.

Liu, L., Zhang, T., Wu, Y., Niu, Z. and Wang, Q.: Cloud Effective Emissivity Retrievals Using Combined Ground-Based Infrared Cloud Measuring Instrument and Ceilometer Observations, Remote Sensing, 10(12), 2033, doi:10.3390/rs10122033, 2018.

5   Lohou, F., Kalthoff, N., Adler, B., Babić, K., Dione, C., Lothon, M., Pedruzo-Bagazgoitia, X. and Zouzoua, M.: Conceptual model of diurnal cycle of low-level stratiform clouds over southern West Africa, Atmospheric Chemistry and Physics, 20(4), 2263–2275, doi:https://doi.org/10.5194/acp-20-2263-2020, 2020.

Lothon, M., Saïd, F., Lohou, F. and Campistron, B.: Observation of the Diurnal Cycle in the Low Troposphere of West Africa, Mon. Wea. Rev., 136(9), 3477–3500, doi:10.1175/2008MWR2427.1, 2008.

Mauder, M., Cuntz, M., Drüe, C., Graf, A., Rebmann, C., Schmid, H. P., Schmidt, M. and Steinbrecher, R.: A strategy for
10 quality and uncertainty assessment of long-term eddy-covariance measurements, Agricultural and Forest Meteorology, 169, 122–135, doi:10.1016/j.agrformet.2012.09.006, 2013.

Mechem, D. B., Kogan, Y. L. and Schultz, D. M.: Large-Eddy Simulation of Post-Cold-Frontal Continental Stratocumulus, J. Atmos. Sci., 67(12), 3835–3853, doi:10.1175/2010JAS3467.1, 2010.

Parker, D. J., Burton, R. R., Diongue-Niang, A., Ellis, R. J., Felton, M., Taylor, C. M., Thorncroft, C. D., Bessemoulin, P.
15 and Tompkins, A. M.: The diurnal cycle of the West African monsoon circulation, Quarterly Journal of the Royal Meteorological Society, 131(611), 2839–2860, doi:10.1256/qj.04.52, 2005.

Pedruzo-Bagazgoitia, X., de Roode, S. R., Adler, B., Babić, K., Dione, C., Kalthoff, N., Lohou, F., Lothon, M. and Vilà-Guerau de Arellano, J.: The diurnal stratocumulus-to-cumulus transition over land in southern West Africa, Atmos. Chem. Phys., 20(5), 2735–2754, doi:10.5194/acp-20-2735-2020, 2020.

20 Prata, A. J.: A new long-wave formula for estimating downward clear-sky radiation at the surface, Q.J Royal Met. Soc., 122(533), 1127–1151, doi:10.1002/qj.49712253306, 1996.

Price, J. D.: Observations of stratocumulus cloud break-up over land, Q.J Royal Met. Soc., 125(554), 441–468, doi:10.1002/qj.49712555404, 1999.

Romps, D. M.: Exact Expression for the Lifting Condensation Level, Journal of the Atmospheric Sciences, 74(12), 3891–
25 3900, doi:10.1175/JAS-D-17-0102.1, 2017.

de Roode, S. R., Sandu, I., van der Dussen, J. J., Ackerman, A. S., Blossey, P., Jarecka, D., Lock, A., Siebesma, A. P. and Stevens, B.: Large-Eddy Simulations of EUCLIPSE–GASS Lagrangian Stratocumulus-to-Cumulus Transitions: Mean State, Turbulence, and Decoupling, J. Atmos. Sci., 73(6), 2485–2508, doi:10.1175/JAS-D-15-0215.1, 2016.

S. Derrien, Y. Bezombes, G. Bret, O. Gabella, C. Jarnot, P. Medina, E. Piques, C. Delon, C. Dione, B. Campistron, P.
30 Durand, C. Jambert, F. Lohou, M. Lothon, F. Pacifico and Y. Meyerfeld: DACCIWA field campaign, Savè super-site, UPS instrumentation, 2016.

Sandu, I. and Stevens, B.: On the Factors Modulating the Stratocumulus to Cumulus Transitions, J. Atmos. Sci., 68(9), 1865–1881, doi:10.1175/2011JAS3614.1, 2011.

Schrage, J. M. and Fink, A. H.: Nocturnal Continental Low-Level Stratus over Tropical West Africa: Observations and
35 Possible Mechanisms Controlling Its Onset, Monthly Weather Review, 140(6), 1794–1809, doi:10.1175/MWR-D-11-00172.1, 2012.

Schuster, R., Fink, A. H. and Knippertz, P.: Formation and Maintenance of Nocturnal Low-Level Stratus over the Southern West African Monsoon Region during AMMA 2006, Journal of the Atmospheric Sciences, 70(8), 2337–2355, doi:10.1175/JAS-D-12-0241.1, 2013.

Stevens, B.: Bulk boundary-layer concepts for simplified models of tropical dynamics, Theor. Comput. Fluid Dyn., 20(5–6),
5   279–304, doi:10.1007/s00162-006-0032-z, 2006.

Stevens, B., Moeng, C.-H., Ackerman, A. S., Bretherton, C. S., Chlond, A., de Roode, S., Edwards, J., Golaz, J.-C., Jiang, H., Khairoutdinov, M., Kirkpatrick, M. P., Lewellen, D. C., Lock, A., Müller, F., Stevens, D. E., Whelan, E. and Zhu, P.: Evaluation of Large-Eddy Simulations via Observations of Nocturnal Marine Stratocumulus, Mon. Wea. Rev., 133(6), 1443–1462, doi:10.1175/MWR2930.1, 2005.

10 Stull, R. B., Ed.: An Introduction to Boundary Layer Meteorology, Springer Netherlands, Dordrecht. [online] Available from: http://link.springer.com/10.1007/978-94-009-3027-8 (Accessed 10 October 2016), 1988.

vanZanten, M. C., Duynkerke, P. G. and Cuijpers, J. W. M.: Entrainment Parameterization in Convective Boundary Layers, J. Atmos. Sci., 56(6), 813–828, doi:10.1175/1520-0469(1999)056<0813:EPICBL>2.0.CO;2, 1999.

Wang, Q. and Lenschow, D.: An Observational Study of the Role of Penetrating Cumulus in a Marine Stratocumulus-
15 Topped Boundary Layer, Journal of The Atmospheric Sciences - J ATMOS SCI, 52, 2778–2787, doi:10.1175/1520-0469(1995)052<2778:AOSOTR>2.0.CO;2, 1995.

Wieser, A., Adler, B. and Deny, B.: DACCIWA field campaign, Savè super-site, Thermodynamic data sets, , doi:10.6096/dacciwa.1659, 2016.

Wood, R.: Stratocumulus Clouds, Mon. Wea. Rev., 140(8), 2373–2423, doi:10.1175/MWR-D-11-00121.1, 2012.

20 Xiao, H., Wu, C.-M. and Mechoso, C. R.: Buoyancy reversal, decoupling and the transition from stratocumulus to shallow cumulus topped marine boundary layers, Clim Dyn, 37(5–6), 971–984, doi:10.1007/s00382-010-0882-3, 2011.

Zhu, P., Albrecht, B. and Gottschalck, J.: Formation and Development of Nocturnal Boundary Layer Clouds over the Southern Great Plains, Journal of the Atmospheric Sciences, 58, doi:10.1175/1520-0469(2001)058<1409:FADONB>2.0.CO;2, 2001.